Clumpy Galaxies in CANDELS. II. Physical Properties of UV-bright Clumps at $0.5 \leqslant z < 3$

Yicheng Guo[1,2] , Marc Rafelski[3] , Eric F. Bell[4] , Christopher J. Conselice[5] , Avishai Dekel[6] , S. M. Faber[1],
Mauro Giavalisco[7] , Anton M. Koekemoer[3] , David C. Koo[1] , Yu Lu[8] , Nir Mandelker[9,10] , Joel R. Primack[11] ,
Daniel Ceverino[12] , Duilia F. de Mello[13] , Henry C. Ferguson[3] , Nimish Hathi[3] , Dale Kocevski[14] , Ray A. Lucas[3] ,
Pablo G. Pérez-González[15], Swara Ravindranath[3], Emmaris Soto[13] , Amber Straughn[16], and Weichen Wang[17]

[1] UCO/Lick Observatory, Department of Astronomy and Astrophysics, University of California, Santa Cruz, CA, USA; ycguo@ucolick.org
[2] Department of Physics and Astronomy, University of Missouri, Columbia, MO 65211, USA; guoyic@missouri.edu
[3] Space Telescope Science Institute, Baltimore, MD, USA
[4] Department of Astronomy, University of Michigan, Ann Arbor, MI, USA
[5] School of Physics and Astronomy, University of Nottingham, University Park, Nottingham NG7 2RD, UK
[6] Center for Astrophysics and Planetary Science, Racah Institute of Physics, The Hebrew University, Jerusalem, Israel
[7] Department of Astronomy, University of Massachusetts, Amherst, MA, USA
[8] Observatories, Carnegie Institution for Science, Pasadena, CA, USA
[9] Department of Astronomy, Yale University, New Haven, CT, USA
[10] Heidelberg Institut für Theoretische Studien, Schloss-Wolfsbrunnenweg 35, 69118 Heidelberg, Germany
[11] Department of Physics, University of California, Santa Cruz, CA, USA
[12] Institut für Theoretische Astrophysik, Zentrum für Astronomie der Universität Heidelberg, Albert-Ueberle-Str. 2, D-69120 Heidelberg, Germany
[13] Physics Department, The Catholic University of America, Washington, DC, USA
[14] Physics and Astronomy Department, Colby College, Waterville, ME, USA
[15] Departamento de Astrofísica, Facultad de CC. Físicas, Universidad Complutense de Madrid, E-28040 Madrid, Spain
[16] Astrophysics Science Division, Goddard Space Flight Center, Code 665, Greenbelt, MD 20771, USA
[17] Department of Physics & Astronomy, Johns Hopkins University, Baltimore, MD, USA

Abstract

Studying giant star-forming clumps in distant galaxies is important to understand galaxy formation and evolution. At present, however, observers and theorists have not reached a consensus on whether the observed "clumps" in distant galaxies are the same phenomenon that is seen in simulations. In this paper, as a step to establish a benchmark of direct comparisons between observations and theories, we publish a sample of clumps constructed to represent the commonly observed "clumps" in the literature. This sample contains 3193 clumps detected from 1270 galaxies at $0.5 \leqslant z < 3.0$. The clumps are detected from rest-frame UV images, as described in our previous paper. Their physical properties (e.g., rest-frame color, stellar mass (M_*), star formation rate (SFR), age, and dust extinction) are measured by fitting the spectral energy distribution (SED) to synthetic stellar population models. We carefully test the procedures of measuring clump properties, especially the method of subtracting background fluxes from the diffuse component of galaxies. With our fiducial background subtraction, we find a radial clump $U - V$ color variation, where clumps close to galactic centers are redder than those in outskirts. The slope of the color gradient (clump color as a function of their galactocentric distance scaled by the semimajor axis of galaxies) changes with redshift and M_* of the host galaxies: at a fixed M_*, the slope becomes steeper toward low redshift, and at a fixed redshift, it becomes slightly steeper with M_*. Based on our SED fitting, this observed color gradient can be explained by a combination of a negative age gradient, a negative $E(B - V)$ gradient, and a positive specific SFR gradient of the clumps. We also find that the color gradients of clumps are steeper than those of intra-clump regions. Correspondingly, the radial gradients of the derived physical properties of clumps are different from those of the diffuse component or intra-clump regions.

1. Introduction

1.1. Overview: Clumps and Their Formation and Evolution

To understand how the morphology and structure of galaxies evolve over cosmic time requires knowledge of not only integrated galaxy properties but also substructures of galaxies. Current facilities enable us to resolve distant galaxies and study their spatially resolved physical properties, including (I) substructures (e.g., Elmegreen & Elmegreen 2005; Elmegreen et al. 2007, 2009a, 2009b; Genzel et al. 2008, 2011; Förster Schreiber et al. 2011; Guo et al. 2012b, 2015; Wuyts et al. 2012; Tadaki et al. 2014; Shibuya et al. 2016; Soto et al. 2017), (II) color variation (e.g., Menanteau et al. 2004; McGrath et al. 2008; Tortora et al. 2010; Gargiulo et al. 2011, 2012; Guo et al. 2011; Szomoru et al. 2011; Boada et al. 2015; Tacchella et al. 2015b; Chan et al. 2016; Liu et al. 2016), (III) star formation variation (e.g., Wuyts et al. 2013; Hemmati et al. 2014, 2015; Tacchella et al. 2015a; Barro et al. 2016; Mieda et al. 2016; Nelson et al. 2016a, 2016b), and (IV) mass distribution and central concentration (e.g., Saracco et al. 2012; Szomoru et al. 2013; Lang et al. 2014; van Dokkum et al. 2014; Barro et al. 2017; Mosleh et al. 2017).

A common and important substructure of distant star-forming galaxies is giant off-center star-forming clumps. These

clumps are seen in deep and high-resolution rest-frame UV and optical images (e.g., Conselice et al. 2004; Elmegreen & Elmegreen 2005; Elmegreen et al. 2007, 2009a; Förster Schreiber et al. 2011; Guo et al. 2012b, 2015; Wuyts et al. 2012; Murata et al. 2014; Tadaki et al. 2014; Shibuya et al. 2016; Soto et al. 2017). They are also detected in high-resolution emission-line maps of Hα (e.g., Genzel et al. 2008, 2011; Wisnioski et al. 2011; Livermore et al. 2012, 2015; Mieda et al. 2016; Fisher et al. 2017a) and CO (e.g., Jones et al. 2010; Swinbank et al. 2010; Dessauges-Zavadsky et al. 2017b). The clumps appear to be much larger, brighter, and more massive than local star-forming regions. Their typical stellar mass (M_*) is 10^7–$10^9 M_\odot$ (e.g., Elmegreen et al. 2007; Guo et al. 2012b; Soto et al. 2017). Their actual sizes are uncertain due to the resolution limit of current observations, ranging from ∼1 kpc (e.g., Elmegreen et al. 2007; Förster Schreiber et al. 2011) to a few hundred pc (e.g., Livermore et al. 2012). The clumps resemble mini-starbursts in their galaxies (e.g., Bournaud et al. 2015; Zanella et al. 2015) and have specific star formation rates (sSFRs) that are higher than those of their surrounding areas by a factor of several, evident by their blue UV–optical colors or enhanced Hα surface brightness (e.g., Guo et al. 2012b; Wuyts et al. 2012, 2013; Hemmati et al. 2014; Mieda et al. 2016).

The formation and evolution of clumps provide important tests of our knowledge of star formation, feedback, and galactic structure formation. Clumps are thought to form through gravitational instability in gas-rich turbulent disks (e.g., Noguchi 1999; Immeli et al. 2004a, 2004b; Bournaud et al. 2007, 2009; Elmegreen et al. 2008; Dekel et al. 2009; Ceverino et al. 2010, 2012; Dekel & Burkert 2014; Inoue et al. 2016). This view is supported by some observations, especially for massive clumpy galaxies (e.g., Elmegreen et al. 2007; Bournaud et al. 2008; Genzel et al. 2008, 2011; Guo et al. 2012b, 2015; Hinojosa-Goñi et al. 2016; Mieda et al. 2016; Fisher et al. 2017a). The kinematic signatures of the clumpy galaxies, however, can also have an ex situ origin, such as gas-rich mergers (e.g., Hopkins et al. 2013), which also has some supporting observations (e.g., Puech et al. 2009; Puech 2010; Wuyts et al. 2014; Guo et al. 2015; Straughn et al. 2015; Ribeiro et al. 2017).

The evolution of clumps is under intense debate. Some models predict that, due to clump—clump and clump—disk interactions and dynamical friction, clumps will migrate toward the gravitational centers of their host galaxies and eventually coalesce into a young bulge as a progenitor of today's bulges (e.g., Bournaud et al. 2007; Elmegreen et al. 2008; Ceverino et al. 2010; Bournaud et al. 2014; Mandelker et al. 2014). Observational evidence of this scenario is the age (or color) variation of clumps with galactocentric distance (clump age gradient). Some studies (e.g., Förster Schreiber et al. 2011; Guo et al. 2012b; Shibuya et al. 2016; Soto et al. 2017) found that clumps close to galactic centers are older than those in the outskirts, broadly consistent with the prediction of the inward migration scenario. In this scenario, clumps need to survive longer than ∼150 Myr to be able to travel to galactic centers.

On the other hand, some models predict a short lifetime of clumps ($\lesssim$50 Myr) because of the quick disruption of clumps by either tidal forces or stellar feedback (e.g., Murray et al. 2010; Genel et al. 2012; Hopkins et al. 2012; Buck et al. 2017; Oklopčić et al. 2017). The disrupted stars from clumps would contribute to the formation of thick disks (e.g.,

Bassett et al. 2014; Inoue & Saitoh 2014; Struck & Elmegreen 2017). Clumps have high sSFR and therefore strong star formation feedback for their M_* (e.g., Genzel et al. 2008; Newman et al. 2012), which enables the quick disruption, although clumps with typical star formation efficiency of a few percent per freefall time are not disrupted (Krumholz & Dekel 2010). Although the observed stellar age gradient and the older-than-100-Myr age of some clumps seem contradictory to the quick disruption scenario, a few simulations (e.g., Buck et al. 2017 and Oklopčić et al. 2017), argue that these observations can be interpreted as clump regions being contaminated by older disk stars and therefore may not be an indicator of the long lifetime and inward migration of clumps.

Understanding the evolution of clumps is important, because it reveals whether clumps are a major contributor to bulge formation, given their prevalence at high redshifts (e.g., Elmegreen et al. 2007; Tadaki et al. 2014; Guo et al. 2015; Shibuya et al. 2016). Clumps may also significantly contribute to the growth of supermassive black holes and active galactic nuclei (AGNs) (e.g., Bournaud et al. 2011; Gabor & Bournaud 2013), which has both supporting (Bournaud et al. 2012; Guo et al. 2012b) and contradicting (Trump et al. 2014) observational evidence.

Whether or not clumps are a major contributor to bulge formation, they are important to further understand star formation feedback, because they provide a sensitive diagnostic of feedback models on sub-galactic scales. Moody et al. (2014) showed that adding radiation pressure to a feedback recipe significantly reduces the number of intermediate-mass clumps ($M_* \lesssim 10^8 M_\odot$) in their adaptive refinement tree (ART) simulations (Kravtsov et al. 1997; Kravtsov 2003; Ceverino & Klypin 2009), compared to having only supernova feedback. Mandelker et al. (2017) further studied the dependence of clump properties and evolution on feedback recipes in detail. They found that including radiation pressure would increase the baryonic surface density and baryonic mass thresholds for clumps that are long-lived and not being disrupted in a few freefall times. In the Feedback In Realistic Environments (FIRE) simulation (Hopkins et al. 2014), where the feedback recipe reduces star formation more than in the ART simulations, clumps are reported to all have short lifetimes of $\lesssim$50 Myr (Oklopčić et al. 2017). Therefore, the properties of clumps (e.g., number, mass, star formation rate (SFR), and age) are important to test the validity of feedback models.

1.2. A Challenge of Clump Studies and the Motivation of This Paper

The resolution and sensitivity of current facilities pose a significant challenge when comparing observations to models and even observations to each other. Even with the *Hubble Space Telescope* (*HST*), clumps at high redshifts can only be marginally resolved or may even be unresolved. This limitation raises the question whether an observed clump is actually a single object or blending of a few nearby smaller clumps. For example, Tamburello et al. (2015) argued that many of the giant clumps (with $M_* > 10^8 M_\odot$) identified in observations are not due to in situ formation but are the result of the blending of smaller structures due to the low resolution of the observations. Similarly, Dessauges-Zavadsky et al. (2017a) claimed that the clump masses observed in non-lensed galaxies

with a limited spatial resolution of ∼1 kpc are artificially increased due to the clustering of clumps of smaller mass. They also stated that the sensitivity threshold used for the clump selection strongly biases against clumps at the low-mass end. Similarly, Fisher et al. (2017b) discussed the effects of clump clustering on kpc-scale measurements of clumps. They inferred that the clustering systematically increases the apparent size and SFR of clumps in 1 kpc resolution maps and decreases the measured SFR surface density of clumps by as much as a factor of 20.

To address the issue of observational effects, in Guo et al. (2015, hereafter Paper I), we proposed a physical definition that UV-bright clumps are off-center discrete star-forming regions that individually contribute more than 8% of the rest-frame UV light of their galaxies. This definition is derived through comparison with redshifted and size-matched nearby spiral galaxies. Clumps defined this way are significantly brighter than the H II regions of nearby large spiral galaxies, either individually or blended, when physical spatial resolution and cosmological dimming are considered. This objective and physical definition enables a consistent study of clumps at different redshifts, complementing clump studies of using the appearance of galaxies by either visual inspection (e.g., Cowie et al. 1995; van den Bergh et al. 1996; Elmegreen et al. 2004, 2007; Elmegreen & Elmegreen 2005) or other automated algorithm (e.g., Conselice 2003; Conselice et al. 2004; Förster Schreiber et al. 2011; Guo et al. 2012b; Wuyts et al. 2012; Murata et al. 2014).

Under this definition, in Paper I, we measured the fraction of star-forming galaxies that have at least one off-center clump (f_{clumpy}). The redshift evolution of f_{clumpy} changes with the M_* of the host galaxies. Low-mass ($\log(M_*/M_\odot) < 9.8$) galaxies keep an almost constant f_{clumpy} of ∼60% from $z \sim 3$ to $z \sim 0.5$. Intermediate-mass ($9.8 \leqslant \log(M_*/M_\odot) < 10.6$) and massive ($\log(M_*/M_\odot) \geqslant 10.6$) galaxies drop their f_{clumpy} from 55% at $z \sim 3.0$ to 40% and 15%, respectively, at $z \sim 0.5$. We found that (1) the trend of disk stabilization predicted by violent disk instability matches the f_{clumpy} trend of massive galaxies; (2) minor mergers are a viable explanation of the f_{clumpy} trend of intermediate-mass galaxies at $z < 1.5$, given a realistic observability timescale; and (3) major mergers are unlikely to be responsible for the f_{clumpy} trend in all masses at $z < 1.5$.

This paper is the second of a series aiming to understand the observational effects of clump studies and hence constructing a direct and unbiased comparison between observation and theory. We measure the physical properties of the clumps detected in Paper I and provide our clump catalog to the community. The goal of this paper is not to use our measurements to test models. Rather, it is to present a sample that, to the best of our knowledge, represents the observed "clumps" in the literature. At present, observers and theorists have not reached a consensus on whether the observed "clumps" are the same phenomenon that is seen in simulations. A critical step of reaching the consensus is to understand the physical properties of the observed clump over wide redshift and mass ranges. Public catalogs containing detailed information on clumps, however, are still insufficient (for example, see the compilation of Dessauges-Zavadsky et al. 2017a). The catalog presented in this paper is our contribution to establishing a benchmark of direct comparisons, providing a data set to allow (1) theorists to understand the observed "clumps" in a

wide range of redshifts and galaxy M_* and (2) observers to examine the observational effects for a large sample of clumps.

In this paper, we briefly summarize the galaxy sample and clump sample in Section 2. In Section 3, we describe the measurement of multiband photometry of individual clumps and test its accuracy. We particularly test the effects of different methods of subtracting the surrounding background of clumps, because the contamination by disk stars is a major uncertainty when interpreting the observed properties. In Section 4, we describe the measurement of the stellar population of clumps. We also present a few sanity checks on the accuracy of the measurement. In Section 5, we show a few examples of the measured physical properties, which we think may be of interest to most readers. In Section 6, we briefly introduce the clump catalog and a few cautions for using it.

Throughout the paper, we adopt a flat ΛCDM cosmology with $\Omega_m = 0.3$, $\Omega_\Lambda = 0.7$ and use the Hubble constant in terms of $h \equiv H_0/100\ \mathrm{km\ s^{-1}\ Mpc^{-1}} = 0.70$. All magnitudes in the paper are in AB scale (Oke 1974) unless otherwise noted. We use a Chabrier initial mass function (IMF; Chabrier 2003).

2. Data and Sample Selection

2.1. Galaxy Sample

The galaxies used in this paper are from the CANDELS/ GOODS-S sample presented in Paper I, which is based on the CANDELS survey (Grogin et al. 2011; Koekemoer et al. 2011). We do not include the CANDELS/UDS sample of Paper I in this paper, because UDS only has four *HST* bands, not enough for carrying out spatially resolved spectral energy distribution (SED) fitting for individual clumps. While referring readers to Paper I for details, we briefly summarize the key selection criteria here.

The multiband photometry catalog of GOODS-S is described by Guo et al. (2013). The photometric redshift (photo-*z*) was measured by the method of Dahlen et al. (2013). The M_* and SFR were measured through SED fitting. CANDELS has generated a unified M_* catalog (Mobasher et al. 2015; Santini et al. 2015), where each galaxy is fit by 12 SED-fitting codes with different combinations of synthetic stellar population models, star formation histories, fitting methods, etc. For each galaxy, we quote the median of the best-fit M_* of the 12 SED-fitting codes as its M_*. We also use the median SFR of the 12 SED-fitting codes as our SFR measurement.

Star-forming galaxies are selected to have $M_* > 10^9\ M_\odot$, sSFR $> 10^{-1}\ \mathrm{Gyr^{-1}}$, and $0.5 \leqslant z < 3$. We also use an apparent magnitude cut of $H_{F160W} < 24.5$ AB to ensure reliable morphology and size measurements of the galaxies. We only use galaxies whose effective radii along the galaxy semimajor axis (SMA) is larger than $0\rlap{.}''2$, because clumps cannot be resolved in smaller galaxies. To minimize the effect of dust extinction and clump blending, we only use galaxies with an axial ratio $q > 0.5$.

After the above selection criteria, and further excluding galaxies that are not covered by the Advanced Camera for Surveys (ACS) images, the sample used for detecting clumps consists of 1655 galaxies (some of them may not contain clumps). As a comparison, the CANDELS/UDS sample in Paper I contains 1584 galaxies.

2.2. Clump Sample

Clump detection is detailed in Paper I. Briefly, clumps are detected in rest-frame near-UV (NUV; $\sim$2800 Å), i.e., ACS F435W at $0.5 \leqslant z < 1.0$, F606W at $1.0 \leqslant z < 2.0$, and F775W at $2.0 \leqslant z < 3.0$. First, the detection image is smoothed. The smoothed image is then subtracted from the original image to make a contrast image. After low-S/N pixels are masked out, only off-center "blobs" are detected from the filtered image as regions with at least five contiguous pixels. We choose rest-frame NUV because it is observed by *HST* filters for the whole GOODS-S field across the redshift range of $0.5 \leqslant z < 3.0$. Some clumps are brighter and more prominent in rest-frame far-UV ($\sim$1500 Å), as found by Soto et al. (2017), which makes far-UV also an efficient band to detect active star-forming clumps. However, deep far-UV observations are only available for about one-third of the area of GOODS-S for galaxies at $0.5 \leqslant z < 1.5$. To increases our sample size, we use the NUV detection in this paper. Future large and deep far-UV surveys are needed to promote studies of far-UV clumps.

In Paper I, we only refer to those "blobs" that contribute at least 8% of the total UV luminosity of their galaxies as clumps (see Section 1 for the relevant discussion). This objective and physical definition is necessary when considering clumps as a distinct feature from normal nearby H II regions and studying the redshift evolution of clumps and clumpy galaxies (as in Paper I). This definition, however, has a few caveats. First, this definition only selects very UV-bright star-forming regions with $f_{\mathrm{LUV}} \equiv L_{\mathrm{clump}}^{\mathrm{UV}}/L_{\mathrm{galaxy}}^{\mathrm{UV}} > 8\%$ and identifies all fainter star-forming regions as non-clumps. This bisection of star-forming regions implies an abrupt change of the properties of star formation regions. Theoretical models, however, predict a wide and continuous distribution of clump properties (e.g., Moody et al. 2014; Mandelker et al. 2017). Second, the number of clumps is predicted to increase toward low luminosity (Mandelker et al. 2017). Excluding fainter star-forming regions results in an incomplete and biased clump sample. Third, the threshold of 8% is determined based on redshifting only one local galaxy (M101) in Paper I and may not fully represent all clumps. In this paper, we tend to be more inclusive and include blobs down to $f_{\mathrm{LUV}} = 3\%$. This inclusion enlarges our clump sample, but it may also include regions that are similar to normal nearby H II regions. We leave it to readers to decide a preferred f_{LUV} threshold. Overall, the sample has 1547 clumps with $f_{\mathrm{LUV}} \geqslant 8\%$, 854 clumps with $5\% \leqslant f_{\mathrm{LUV}} < 8\%$, and 792 with $3\% \leqslant f_{\mathrm{LUV}} < 5\%$. In total, 3193 clumps are detected from 1270 galaxies. Figure 1 shows these clumpy galaxies in the SFR–M_* and SMA–M_* diagrams.

2.3. Selection Effects

To detect clumps in rest-frame NUV, we use different *HST* bands at different redshifts: F435W (B) at $0.5 \leqslant z < 1$: F606W (V) at $1 \leqslant z < 2$: and F775W (i) at $2 \leqslant z < 3$. The clump detection is affected by the sensitivities of the three bands. Paper I shows that the clump magnitude of 50% completeness of our detection is about 28.5, 28.5, and 27.8 AB in B, V, and i, respectively. As a result, fainter clumps are harder to detect at higher redshifts.

A more relevant way to evaluate the incompleteness is calculating it as a function of f_{LUV} rather than a function of the clump apparent magnitude. Our clump definition is based on f_{LUV} because (1) our clump finder detects clumps from a contrast image, showing how bright the clumps are relative to their host galaxies, and (2) using a relative ratio of an intrinsic parameter enables direct comparisons between observations with different sensitivities. Paper I shows that at $0.5 \leqslant z < 1.0$, $1.0 \leqslant z < 2.0$, and $2.0 \leqslant z < 3.0$, the 50% completeness occurs at $f_{\mathrm{LUV}} = 0.03$, 0.06, and 0.10, respectively. A large fraction of clumps with low f_{LUV} is missed in our clump detection at high redshift. For example, we might miss 90% of clumps with $f_{\mathrm{LUV}} = 0.03$ at $z > 2$. This effect raises an important caution of using our clump catalog: it is a "representative" rather than a "complete" catalog. Incompleteness needs to be taken into account when deriving measurements that require a complete sample, e.g., the stellar mass function of clumps.

Specifically, our relative definition of clumps, namely, selecting clumps based on f_{LUV} rather than on their absolute luminosity, would introduce two biases. The first is a redshift-dependent bias. At high redshifts, only high f_{LUV} clumps are detected. Therefore, statistical results of clump properties are dominated by high f_{LUV} clumps. Moreover, high f_{LUV} clumps at high redshifts are intrinsically much brighter or more luminous than the corresponding (i.e., same f_{LUV}) clumps at lower redshift. In contrast, at low redshifts, statistical results are contributed by all f_{LUV} clumps. To help readers to evaluate this effect, we list the number of clumps with different f_{LUV} at different (z, M_*) bins in Table. 1.

The second bias is introduced by the total UV luminosity of galaxies with different M_*. Massive star-forming galaxies have higher UV luminosity than lower-mass galaxies. Clumps detected from massive galaxies are therefore intrinsically UV brighter than those from lower-mass galaxies. In other words, intrinsically faint clumps can only be selected from low-UV-luminosity galaxies. In contrast, from UV-bright galaxies, only UV-bright clumps can be selected. This bias would mainly affect comparisons of the distributions of clump properties (e.g., SFR distribution) between galaxies with different M_*. Both biases are introduced because for a given f_{LUV} class, the absolute clump UV luminosity may vary considerably among the different redshift and/or galaxy M_* ranges. The robustness of our results against both biases can be tested by calculating the results using clumps with different f_{LUV} separately (see Section 5.2).

3. Multiband Clump Photometry

For each clump, we measure its multiband photometry from *HST* images in the bands of F435W, F606W, F775W, F814W, F850LP, F105W, F125W, F140W,[18] and F160W. The *HST* images have the capability to resolve at the kpc scale at $0.5 \leqslant z < 3.0$. We use the IRAF/PSFMATCH package to match the point spread functions (PSFs) of all the bands to that of F160W, whose FWHM is about $0\rlap{.}''17$. Details of the PSF-matching method are described in Guo et al. (2011, 2013). As shown in Figure 5 of Guo et al. (2013), for an aperture of 3 pixels, the accuracy of the PSF matching is within 5%.

For each clump, we use an aperture of $0\rlap{.}''18$ (3 pixels) to measure the flux in each band. We then multiply all the fluxes by a factor of 1.5 for the aperture correction. This factor is derived through the curve of growth of the F160W PSF (see the middle panel of Figure 5 of Guo et al. 2013). This method

---

[18] This band was taken by 3D-*HST* (Brammer et al. 2012).
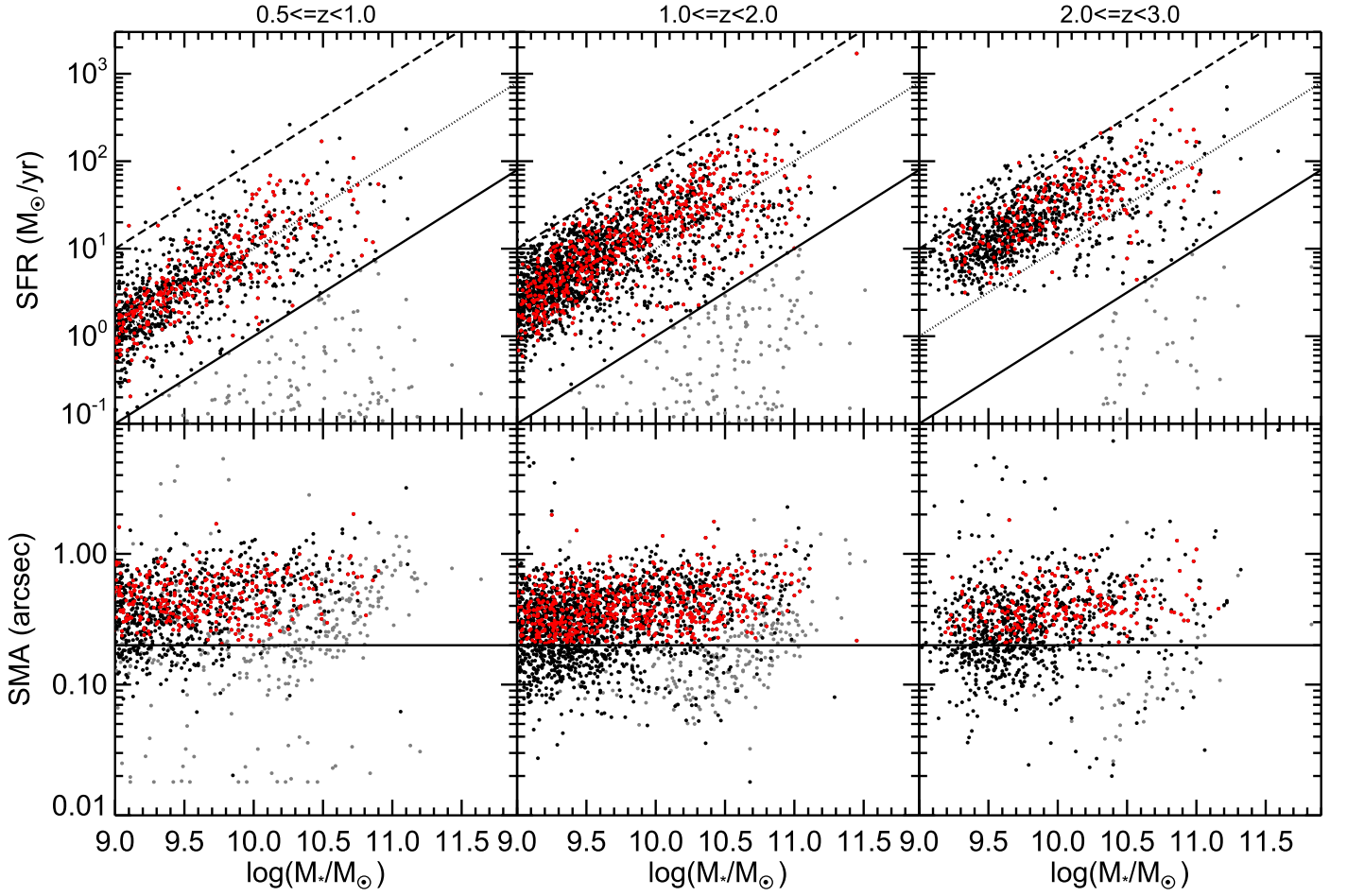
Figure 1. Clumpy galaxy sample split into three redshift bins. Galaxies in the CANDELS/GOODS-S with $H_{F160W} < 24.5$ AB are plotted in the SFR–M_* and SMA–M_* diagrams. Galaxies with sSFR $> 0.1 \mathrm{Gyr}^{-1}$ are black, while those with sSFR $\leqslant 0.1 \mathrm{Gyr}^{-1}$ are gray. Galaxies with at least one detected off-center clump (with $f_{LUV} \equiv L_{clump}^{UV}/L_{galaxy}^{UV} \geqslant 3\%$) are red. The red points all have an axial ratio $q > 0.5$. Black solid, dotted, and dashed lines in the upper panels show the relations of sSFR = 0.1, 1, and 10 Gyr^{-1}. Black horizontal lines in the lower panels show our size cut of $0\rlap{.}''2$.

Table 1
Number of Clumps in the Sample

|	$\log(M_*^{gal}/M_\odot) < 9.8$[a,b]	$9.8 \leqslant \log(M_*^{gal}/M_\odot) < 10.6$	$\log(M_*^{gal}/M_\odot) \geqslant 10.6$
$0.5 \leqslant z < 1.0$	230 galaxies	113 galaxies	16 galaxies
	654 clumps	304 clumps	38 clumps
	171/198/285	107/83/114	13/16/9
$1.0 \leqslant z < 2.0$	363 galaxies	239 galaxies	67 galaxies
	947 clumps	658 clumps	140 clumps
	182/273/492	218/173/267	60/32/48
$2.0 \leqslant z < 3.0$	93 galaxies	127 galaxies	22 galaxies
	181 clumps	230 clumps	41 clumps
	10/25/146	26/45/159	5/9/27

Notes.
[a] M_*^{gal} means M_* of host galaxies.
[b] In each (M_*^{gal}, z) bin, the three numbers in the third row are the numbers of clumps in three f_{LUV} bins: 0.03–0.05, 0.05–0.08, and >0.08.

assumes that each clump is an unresolved source, which is reasonable for the *HST* resolution in F160W, because the FWHM of F160W ($0\rlap{.}''17$) corresponds to ~1 kpc (~1.4 kpc) at $z = 0.5$ (at $1.5 \lesssim z \lesssim 3.0$). The assumption of an unresolved source makes it easy to calculate the clump light that is out of our fixed aperture.

3.1. Diffuse Background Subtraction

A challenge is how to subtract the light from the underlying diffuse component (or intra-clump regions) of the galaxies. Clumps are believed to be "embedded" in a diffuse background. Therefore, in a clump location, the observed light is contributed by both clump stars and background stars.
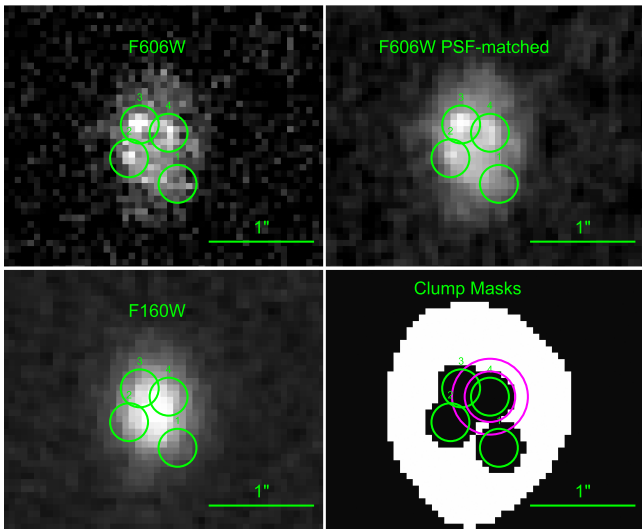
Figure 2. Illustration of diffuse light subtraction. A galaxy (Galaxy ID = 25508 in the catalog) is shown in ACS F606W used to detect clumps (top left), smoothed ACS F606W to match the resolution of WFC3 F160W (top right), WFC3 F160W (bottom left), and a mask image (bottom right). Four clumps are detected in this galaxy, as shown by the green circles with a radius of $0{\farcs}18$ (3 pixels) in each panel. In the mask image (bottom right), the area within $0{\farcs}24$ (4 pixels) of the center of each clump is masked out (i.e., black pixels in the panel). These pixels are not used in calculating the diffuse background. The pixels outside the galaxy are also masked out, because they are out of the SExtractor segmentation map of the galaxy. For one clump (Clump ID = 4 in the catalog), we show the annulus (magenta circles) used as our fiducial method (bgsub_v4 in Table 2) to measure the surface brightness of the diffuse background (or intra-clump regions). The annulus (between the two magenta circles) has inner and outer radii of $0{\farcs}24$ and $0{\farcs}36$. Only the white pixels (i.e., those not masked out due to clump locations) between the two magenta circles are used to calculate the surface brightness of the diffuse background.

Separating the two contributions is scientifically critical. Some numerical simulations (e.g., Buck et al. 2017; Oklopčić et al. 2017) found a radial variation of clump ages: older for inner (small galactocentric distance) clumps and younger for outer (large galactocentric distance) clumps, which seems to support the inward migration scenario (see discussion in Section 1). These simulations, however, found no clump migration, and they argued that the clump age gradient in their simulations is the result of the contamination of disk (i.e., background) stars. To make a direct comparison with models, background subtraction is important to eliminate the contamination.

Observationally, subtracting the diffuse background is important for measuring clump photometry. After PSF matching to the F160W resolution, some clumps may disappear due to the reduced contrast between clumps and the background. Moreover, some intrinsically blue clumps are almost "invisible" in red bands (e.g., F160W), again due to small clump–background contrasts (e.g., see clumps in Figure 2 and discussion in Soto et al. 2017). For these clumps, we fix their centers as those detected in the non-PSF-matched NUV bands to measure the aperture photometry. The accuracy of the photometry significantly relies on the precision of the diffuse background subtraction, because the photometry is in fact the measurement of the "excess" flux above the diffuse background flux.

To subtract the diffuse background light, in each band, we first mask out the locations of all detected clumps with circular masks. Then, for each clump, we measure the background flux from an annulus around the clump to calculate the average local background surface brightness (i.e., flux per pixel) in the clump vicinity. We then subtract the background flux within the clump aperture of $0{\farcs}18$ (i.e., the local background surface brightness times the clump area). The subtracted background for the clump is contributed by two sources: the local diffuse background and the PSF wings of nearby clumps and the analyzed clump itself. Figure 2 illustrates the method.

Two parameters control this method: (1) the size (radius) of the clump mask and (2) the size of the background annulus. We try different combinations of them (see Table 2). For an aggressive subtraction (e.g., bgsub_v6), the clump mask size is small, leaving more pixels as background (or intra-clump) pixels, and the background annulus starts right next to the clump region. In contrast, a conservative subtraction (e.g., bgsub_v1) masks more pixels as clump regions and measures the background far away from the clump regions. As shown in Table 2, the difference between aggressive subtraction (bgsub_v6) and conservative subtraction (bgsub_v1) is about a factor of 1.9 in clumps' F160W flux. If no background is subtracted (bgsub_v0), the F160W flux of clumps is about a factor of 3.2 higher than that of bgsub_v6. Here we use F160W flux to show the effect of background subtraction, because this issue is most significant in F160W due to the faint clump fluxes in this band.

We choose method bgsub_v4 as our fiducial one based on a test of fake clumpy galaxies. In this test, we use the WFC3 F160W PSF as fake clumps and insert four fake clumps into a constant diffuse background. For each fake galaxy, we choose one clump as the target clump and normalize its flux to unity. The fluxes of other fake clumps are randomly drawn from the range of 0.1–10 relative to the flux of the target clump. The separation between the fake clumps is drawn from the observed distribution of clump–clump distances. The surface brightness of the constant background ranges from 0.01% to 10% of the peak surface brightness of the target fake clump.

We apply all subtraction methods to the fake galaxies and test which one recovers the input flux of the target clump the best. The most affecting parameter in this test is the flux ratio between the target fake clump and its closest neighbor. On average, method bgsub_v4 recovers the target flux the best over the range of the clump flux ratio. It recovers $\gtrsim$95% of the target flux when the neighbor clump is not brighter than the target one by a factor of 2. It overestimates the target flux by a factor of 1.1 when the neighbor clump is five times brighter.

Background subtraction, however, is more complicated than the above test. Technically, a few issues are not covered by the test. First, some clumps may be more extended than WFC3 PSFs. Second, the diffuse background is not constant in the galaxy-size scale. Third and more importantly, different clumps have different distances to their neighbor clumps and different clump-to-neighbor flux ratios, which means the best background-subtraction configuration may vary from clump to clump.

Physically, whether or not the background should be subtracted depends on the scientific goals. For example, if the goal is to study the clump properties (e.g., mass, SFR, etc.), the background needs to be subtracted. If, however, the goal is to study the dynamics of clump regions, the background should be kept. To enable as many topics as possible, we release the clump catalogs with all the background-subtraction methods (including no subtraction), allowing readers to choose the optimal method for their research. Moreover, the very

Table 2
Diffuse Background Measurement

Method	Clump Mask Size[a] (arcsec)	Background Aperture[b] (arcsec)	Median Relative F160W Flux[c] (normalized)	Photo-z $\sigma_{\rm NMAD}$[d,e]	Photo-z Outlier[f]	Comment
bgsub_v6	0.18	0.18–0.30	0.67	0.114	6.99%	Very aggressive subtraction
bgsub_v5	0.18	0.24–0.36	0.86	0.088	6.86%	⋯
bgsub_v4	0.24	0.24–0.36	1.00	0.074	6.66%	Fiducial subtraction
bgsub_v3	0.24	0.24–0.42	1.08	0.072	6.59%	⋯
bgsub_v2	0.24	0.30–0.42	1.14	0.073	6.55%	⋯
bgsub_v1	0.24	0.36–0.48	1.25	0.063	6.44%	Very conservative subtraction
bgsub_v0	⋯	⋯	2.17	0.042	5.76%	No background subtraction

Notes.
[a] The radius of clump regions masked out when calculating the diffuse background (see green circles in Figure 2). One pixel is $0''06$.
[b] The inner and outer radii of the aperture used to measure the diffuse background (see the magenta circles in Figure 2).
[c] Median of clumps' F160W fluxes normalized by those of bgsub_v4.
[d] NMAD: normalized median absolute deviation; $\sigma_{\rm NMAD} = 1.48 \times (|\Delta z - {\rm median}(\Delta z)|/(1 + z_{\rm spec}))$, where $\Delta z = z_{\rm photo} - z_{\rm spec}$.
[e] Only use clumps with spec-z and $f_{\rm LUV} \geqslant 0.08$.
[f] Outliers are defined as $|\Delta z|/(1 + z) > 0.15$.

aggressive subtraction (bgsub_v6) and no subtraction (bgsub_v0) can be used as the lower and upper limits of clump fluxes to evaluate the uncertainty caused by subtracting the diffuse background. The "fiducial" method (bgsub_v4) is chosen to simplify the paper, focusing on the clump properties. We will discuss the effects of background subtraction on clump properties more in Section 5.7.

3.2. Accuracy of Photometry

Background subtraction affects photometric accuracy. An aggressive method (e.g., bgsub_v6) subtracts a higher fraction of light from clumps than a conservative method does. In the former, the remaining clump flux is fainter, and the relative error of the clump flux is therefore larger (or the clump S/N is lower). To test the photometric accuracy, we measure the photo-zs of individual clumps by using their *HST* photometry. The code and details of our photo-z method are described in Guo et al. (2012a). Models used to measure photo-zs are extracted from the library of PEGASE 2.0 (Fioc & Rocca-Volmerange 1997). For integrated galaxies, our photo-z code achieves a similar accuracy as those used in official CANDELS photo-z catalogs (Dahlen et al. 2013). To test the photo-z accuracy of clumps, we only use clumps with spectroscopic redshifts (spec-zs) and $f_{\rm LUV} > 8\%$.

Table 2 shows that when the background subtraction is too aggressive (e.g., bgsub_v6), the scatter (the normalized median absolute deviation $\sigma_{\rm NMAD}$) and outlier (defined as sources with $|\Delta z|/(1 + z) > 0.15$) fraction of the photo-$z$ measurement are large. In contrast, conservative (or no) subtraction (bgsub_v1 or bgsbu_v0) yields much improved photo-z statistics.

The photo-z result of the fiducial subtraction method is shown in Figure 3. The $\sigma_{\rm NMAD}$ (normalized median absolute deviation) and outlier fraction of bgsub_v4 are 0.074 and 6.66%, both of which are about a factor of 2.5 larger than the values of the CANDELS official photo-z catalogs of Dahlen et al. (2013). Worse photo-z accuracy of clumps is expected because (1) clumps are much fainter than integrated galaxies (e.g., see Figure 4); (2) clumps only have photometry of a few *HST* bands, while integrated galaxies usually have more than 15 bands; (3) clump photometry only samples the relatively featureless regime of the SEDs of star-forming population

models, i.e., rest-frame UV–optical without a strong Balmer/D4000 break; and (4) background subtraction itself induces a source of uncertainty. Considering all these factors, the photo-z accuracy is acceptable. In this paper, clump photo-zs are only used for the purpose of testing their photometry. They are not used for deriving clump properties. We use the redshifts of the host galaxies to derive clump properties.

Some clumps have catastrophic photo-z measurements with $|\Delta z|/(1 + z) > 0.20$ (dashed lines in Figure 3), which may indicate problematic photometry. We exclude such clumps in our later analyses but still keep them in the published catalog. We set a flag *badczflag = 1* in the catalog to label these clumps. In total, 720 (out of 3193) clumps are thereby excluded. Among the 720 clumps, 264, 187, and 269 clumps have UV fractional luminosity $f_{\rm LUV} \geqslant 0.08$, $0.05 \leqslant f_{\rm LUV} < 0.08$, and $0.03 \leqslant f_{\rm LUV} < 0.05$, respectively.

4. Measuring Clump Properties

4.1. SED Fitting

We derive the physical properties (M_*, SFR, age, and dust reddening) of clumps by fitting their *HST* SEDs to stellar population synthesis models retrieved from the library of Bruzual & Charlot (2003) with a Chabrier IMF (Chabrier 2003). The details of our SED-fitting code are described in Guo et al. (2012a). Briefly, we use a set of τ-models in which star formation history (SFH) declines exponentially with time. The set of models consists of grid points in a parameter space spanned by redshift, dust extinction $E(B - V)$, SFH characterized by τ and age, and metallicity. The available values of each parameter are shown in Table 3. We apply the Calzetti extinction law (Calzetti et al. 1997, 2000) and the recipe of Madau (1995) to the models to account for dust extinction and the opacity of the intergalactic medium (IGM) in the universe. We use the minimal χ^2 value to decide the best-fit model. During the SED fitting, the redshift of a clump is fixed to that of its host galaxy (spec-z if available, photo-z otherwise). For each clump, we Monte Carlo sample its photometry in each band 100 times from a Gaussian distribution whose mean is equal to the observed flux and whose standard deviation is equal to the flux uncertainty. We then fit the 100 resampled SEDs. For each stellar population parameter, the average of the
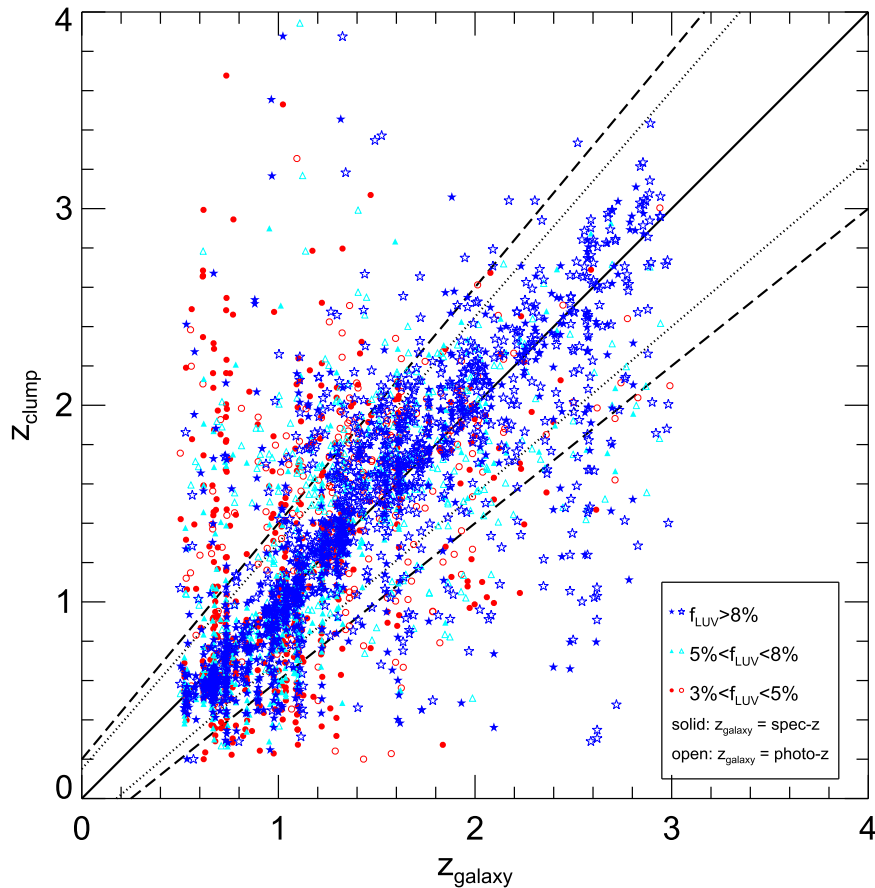
Figure 3. Comparison between the photo-zs of clumps and the redshifts of their host galaxies. The photo-zs of clumps are measured through *HST*-band PSF-matched photometry (see the text). Our fiducial background-subtraction method bgsub_v4 (see Table 2) is used. Blue stars, cyan triangles, and red circles show clumps with UV fractional luminosity $f_{LUV} \equiv L_{clump}^{UV}/L_{galaxy}^{UV} > 0.08$, $0.05 < f_{LUV} < 0.08$, and $0.03 < f_{LUV} < 0.05$. For each color, the solid symbols show the clumps whose host galaxies have high-quality spectroscopic redshifts, while open symbols show the clumps whose host galaxies only have photo-zs from CANDELS. The solid line shows the one-to-one correspondence, while the two dotted lines show $|\Delta z|/(1 + z) = 0.15$, which is used to calculate the outlier fraction. The two dashed lines show $|\Delta z|/(1 + z) = 0.2$. Clumps whose photo-zs are worse than this criterion may have inaccurate multiband photometry and hence are excluded from our later analyses.

100 best-fit values is used as the best value, and the 16th and 84th percentiles of the 100 best-fit values are used as the 1σ confidence level.

SED-fitting results significantly rely on the assumed SFHs. Unfortunately, the SFHs of clumps are little known. Here we choose the τ-model and constant SFH model because they are commonly used in the SED fitting of distant galaxies. Recently, other models (e.g., the inverse τ-model and delayed τ-model) have also been frequently used in the literature. An unrealistic SFH model would result in systematic errors of the derived parameters, especially for age. Lee et al. (2017) tested the effects of different models on the derived parameters for integrated CANDELS galaxies. They generated mock SEDs with known intrinsic parameters and fit the SEDs with different SFH models. They found that (1) M_* is the most robust parameter and nearly unaffected by the adapted models; (2) the constant SFH recovers age (defined as the period from the onset of star formation to the time the object is observed) with little systematic offset, while the τ-model underestimates age by ~ 0.3 dex (for a system of $\lesssim 1$ Gyr old); and (3) for systems with SFR $> 0.01\,M_\odot\,\mathrm{yr}^{-1}$, the constant SFH overestimates SFR by 0.25 dex, while the τ-model recovers SFR with little systematic offset. We expect similar systematic errors due to SFH assumptions in our clump SED fitting. However, since our data cover a much shorter wavelength range and have larger

photometric uncertainties, the random errors of our clump SED fitting are larger than integrated galaxy SED fitting. We do not find any systematic trend between clump age and the SED-fitting preferred SFHs.

4.2. Tests of Clump Properties. I. Mass-to-light Ratio

We test the accuracy of clump properties in three ways. The first is the mass-to-light ratio (M/L). Among all *HST* bands, F160W is the reddest and therefore serves as the best M_* indicator in our method. We expect that the M/L of clumps is similar to or slightly smaller than that of integrated galaxies at a given M_*, because clumps are believed to be younger. In Figure 4, we plot the relation between M_* and F160W magnitude for clumps and integrated CANDELS/GOODS-S galaxies. In each panel, we plot clumps that are detected from galaxies within a given M_* and redshift range (as shown by the label and dotted horizontal lines in each panel), but we also plot all CANDELS/GOODS-S galaxies (not just our sample galaxies), regardless of their M_*, within the redshift range.

Clumps follow a similar relation with integrated galaxies. This result is especially true at $0.5 \leqslant z < 1.0$, when F160W is sampling ~ 9000 Å, very close to the peak of stellar emission. In this redshift range, the variation of M/L caused by different stellar populations is the smallest. At higher redshifts, the M/L of clumps is slightly smaller than that of integrated galaxies,
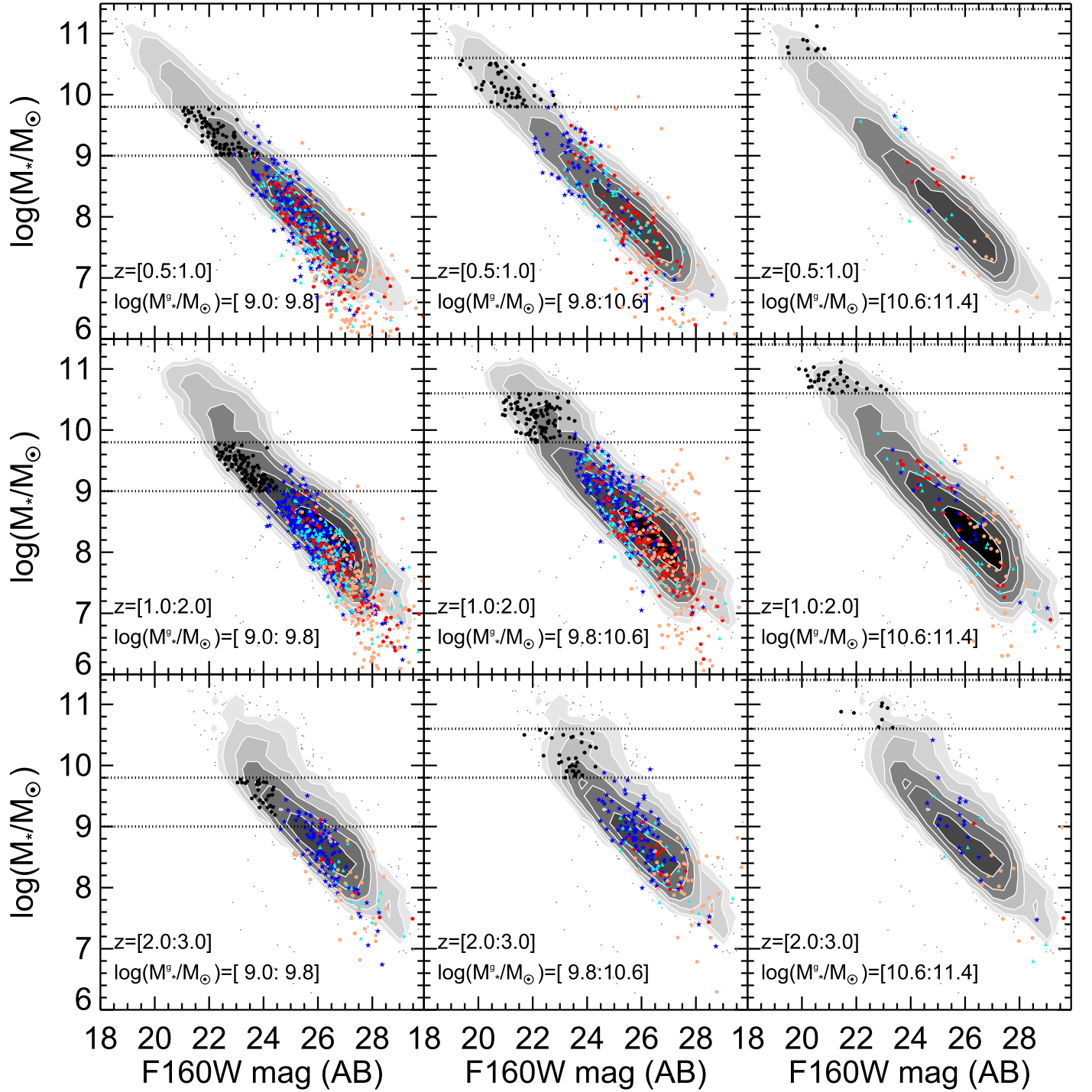
Figure 4. M_*–magnitude (F160W) diagram of clumps. Each panel shows clumps detected from galaxies within a given M_* and redshift bin as the labels indicate. Similar to Figure 3, in each panel, blue, cyan, and red clumps have $f_{LUV} \equiv L_{clump}^{UV}/L_{galaxy}^{UV} > 0.08$, $0.05 < f_{LUV} < 0.08$, and $0.03 < f_{LUV} < 0.05$, respectively. The orange clumps are those excluded because of their large photo-z errors $|\Delta z|/(1 + z) > 0.2$. The gray contours and points show the distribution of all CANDELS/ GOODS-S galaxies (not just our sample galaxies) within the same redshift range of each panel but simultaneously for all mass ranges. In each panel, the two horizontal dotted lines show the M_* range of the host galaxies. The black dots in each panel show the host galaxies of detected clumps.

demonstrated by the fact that clumps are lying toward the lower boundary of the galaxy M_*–magnitude relation. The difference could be caused by a bandpass coverage effect. At $z \geqslant 1$, *HST* filters are shifted to cover a bluer side of the SED than at $z < 1$, probing more of the young star component and less of the old star component. As a consequence, our clump mass measurement is likely overweighting the UV luminosity and artificially biasing the M/L to lower values. The difference, however, is

small, because galaxies with M_* similar to that of clumps at $z > 1$ are also very actively forming stars. Overall, this test shows that there are no obvious, significant systematics in the M_* measurement of clumps. Also, the large scatter of clumps with bad clump photo-z (i.e., those with *badczflag = 1*; orange circles in the figure) supports our decision of not including them in later analyses, because their problematic photometry causes large uncertainties in M_*.

Table 3
Parameter Space of SED Fitting

Parameter	Range
Redshift	0.0 to 7.0 with a bin size of 0.01
$E(B - V)$[a]	0.0 to 1.0, $\Delta E(B - V) = 0.05$
Metallicity	Solar
Age (Gyr)[b]	$(1, 2, 3, 5, 8) \times 10^{-2}$, 10^{-1}, 10^{0}, 10^{1}, up to 13
τ (Gyr)	$(1, 2, 3, 5, 8) \times 10^{-1}$, 10^{0}, 10^{1}, and ∞[c]

Notes.
[a] $E(B - V)$ runs up to 0.3 for models with $t/\tau >= 4.0$.
[b] Age is defined as the period from the onset of star formation (i.e., the beginning of the τ-model or constant SFH model) to the time the object is observed.
[c] $\tau = \infty$ means a constant SFH.

(This table is available in its entirety in machine-readable form.)

4.3. Tests of Clump Properties. II. Color–mass Diagram

The second test is the color–M_* diagram. In Figure 5, we plot both clumps and integrated galaxies in the diagram of rest-frame $U - V$ versus M_*. Clumps have similarly blue colors as those galaxies whose M_* is comparable to the clump M_*, but clumps are bluer than their host galaxies. This result is expected, since clumps are selected as UV-bright regions from their galaxies. At a given redshift and galaxy M_*, clump colors show a relation with their M_*: massive clumps are redder than lower-mass clumps. Also, for a given clump mass, UV-bright clumps (blue stars) are bluer than UV-faint clumps (red dots), as expected. We also notice that some clumps are as red as red-sequence galaxies, i.e., above the separation line of the blue cloud and the red sequence of integrated galaxies from Borch et al. (2006): $(U - V) = 0.227 \times \log(M_*/M_\odot) - 1.16 - 0.352 \times z + (0.79 - 0.02)$, where the last term is to convert the Vega magnitude in Borch et al. (2006) to AB. The very red colors may indicate problematic photometry, because our clump identification is designed to select star-forming (and implicitly low dust extinction) clumps. We therefore exclude all clumps above the separation line (solid black lines in Figure 5) in our later analyses. In the catalog, we set a flag *veryredflag = 1* to label them. The fraction of the *veryredflag = 1* clumps increases with redshift: ∼1% at $0.5 \leqslant z < 1.0$, ∼7% at $1.0 \leqslant z < 2.0$, and ∼8% at $2.0 \leqslant z < 3.0$. This result is likely caused by the filter coverage: at higher redshift, *HST* filters are shifted to cover bluer wavelengths, resulting in large uncertainties in the measure of the rest-frame *V*-band luminosity. In total, 142 clumps are thereby excluded (after *badczflag = 1* is applied), reducing the clean sample to 2331 clumps.

4.4. Tests of Clump Properties. III. SFR and $E(B - V)$

The third test is clump SFR and dust extinction $E(B - V)$. In addition to the SED fitting, we also estimate the SFRs and $E(B - V)$s of clumps by using the slope and luminosity of their rest-frame UV continuum. Compared to SED fitting, this method is less model-dependent and requires no prior information on the SFH of galaxies. We first calculate the UV slope through a linear fit of $\log(f) \propto \beta\lambda$, where f is flux, λ is wavelength, and β is the UV slope. We then use the Calzetti extinction law (Calzetti et al. 1994, 2000) to convert the

rest-frame UV slope of a clump into its dust-reddening $E(B - V)$ and calculate the unobscured SFR from its dust-corrected rest-frame UV continuum by using the formula in Kennicutt (1998), which applies to systems with constant star formation over timescales of ∼100 Myr. The rest-frame UV continuum used here covers the wavelength range of 1400–2800 Å. We require the clumps to have at least two *HST* bands to sample this range. Under this requirement, the bluest *HST* band in our data set (F435W) only enables the measurement of UV SFRs for clumps at $z \gtrsim 1.5$. Therefore, although the UV SFR is less model-dependent than the SED-fitting-derived SFR, we only use the former to test the latter. For the whole clump sample, we still use SED-fitting-derived SFRs as our measurement.

Figure 6 shows very good agreement between SED-fitting- and UV-continuum-derived SFRs and $E(B - V)$s. The average difference between SED and UV SFRs (ΔSFR $= \log(\text{SFR}_{\text{SED}}) - \log(\text{SFR}_{\text{UV}})$) is about 0.07 dex, and the 1σ scatter of ΔSFR is about 0.4 dex—slightly larger than the typical SFR uncertainty for integrated galaxies in the literature. For $E(B - V)$, the average difference is about 0.02, and the 1σ scatter is about 0.1. The agreement in the higher-redshift range $2.0 < z < 3.0$ is better than that in the lower range $1.5 < z < 2.0$, because in the former, three or more *HST* bands are sampling the rest-frame UV continuum, enabling a more accurate measurement, while in the latter, only two *HST* bands are available.

Overall, the above tests find no obvious and significant systematics in our measurements of clump properties. Some major stellar population parameters—M_*, SFR, and $E(B - V)$—are measured to a reasonable accuracy level. All of these tests also provide criteria to exclude problematic clumps from the sample. As a summary, we exclude clumps that have (1) bad photo-z (*badczflag = 1*) or (2) very red $U - V$ color (*veryredflag = 1*).

4.5. Tests of Clump Properties. IV. Comparison with Integrated Values

We also carry out two additional sanity checks to use the integrated values as constraints on clump properties. For each galaxy, (1) the total M_* in clumps should be lower than the integrated M_* of the host galaxy and (2) the total SFR in clumps should be smaller than the integrated SFR of the host galaxy. These tests provide additional information on the robustness of our measurements. We only use the clean sample of 2331 clumps (see Section 4.3) for this test.

In our fiducial background-subtraction method (bgsub_v4), 13 galaxies (1% of the total 1270 galaxies) fail the total clump mass test, while 32 galaxies (3% of the total galaxies) fail the total SFR test. The reasons of failure, however, are different between the mass and SFR tests. Among the 13 failed galaxies in the mass test, only two of them have a single clump that is more massive than the integrated galaxy (such clumps are flagged with *badmassflag = 1* in the catalog). In the SFR test, however, 21 of 32 failed galaxies contain a single clump with SFR larger than the integrated SFR of the galaxies. If we exclude these 21 clumps with overestimated SFR, only 11 galaxies (1%) fail the SFR test. The failure fraction also depends on the background subtraction, with aggressive subtraction resulting in less failure galaxies or clumps.
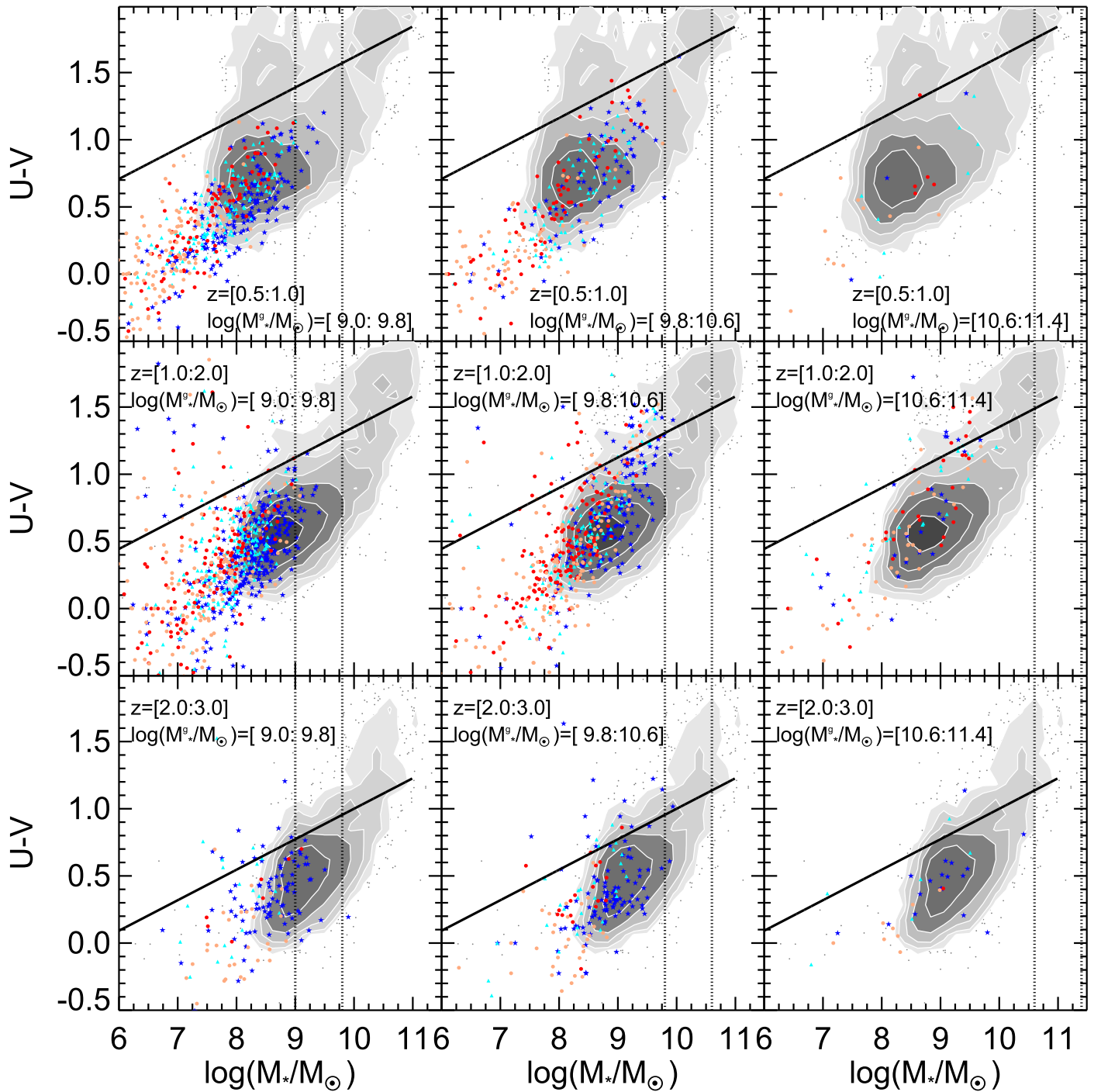
Figure 5. Similar to Figure 4 but showing the color–M_* diagram of clumps (color symbols) and CANDELS/GOODS-S galaxies (gray contours and points). The solid line in each panel is the separation between the red sequence and blue cloud derived in Borch et al. (2006). In each panel, the two vertical dotted lines show the M_* range of the host galaxies where clumps are identified (see also the M_* label).

5. Observed Clump Properties

In this section, we present some observed clump properties that may be of interest to readers. We only present these results and discuss their systematics and uncertainties. The theoretical interpretations and implications of the observed clump properties are beyond the scope of this paper and are thereby left for future work. In most figures in this section, we divide our sample into different redshift and galaxy M_* bins (same as in Figures 4 and 5). The symbols and colors in these figures are also the same as in Figures 4 and 5 unless otherwise stated. All

of these properties are measured with our fiducial diffuse background subtraction bgsub_v4 (see Table 2).

5.1. Specific Star Formation Rate versus M_*

Figure 7 shows the relation between sSFR and M_* for clumps (colored symbols) and integrated CANDELS/ GOODS-S galaxies with F160W < 26 AB (gray contours and points). In most panels, the sSFR of clumps increases with the decrease of clump M_*. In contrast, galaxies below $10^{10} M_\odot$ have an almost constant sSFR, evident by the almost horizontal
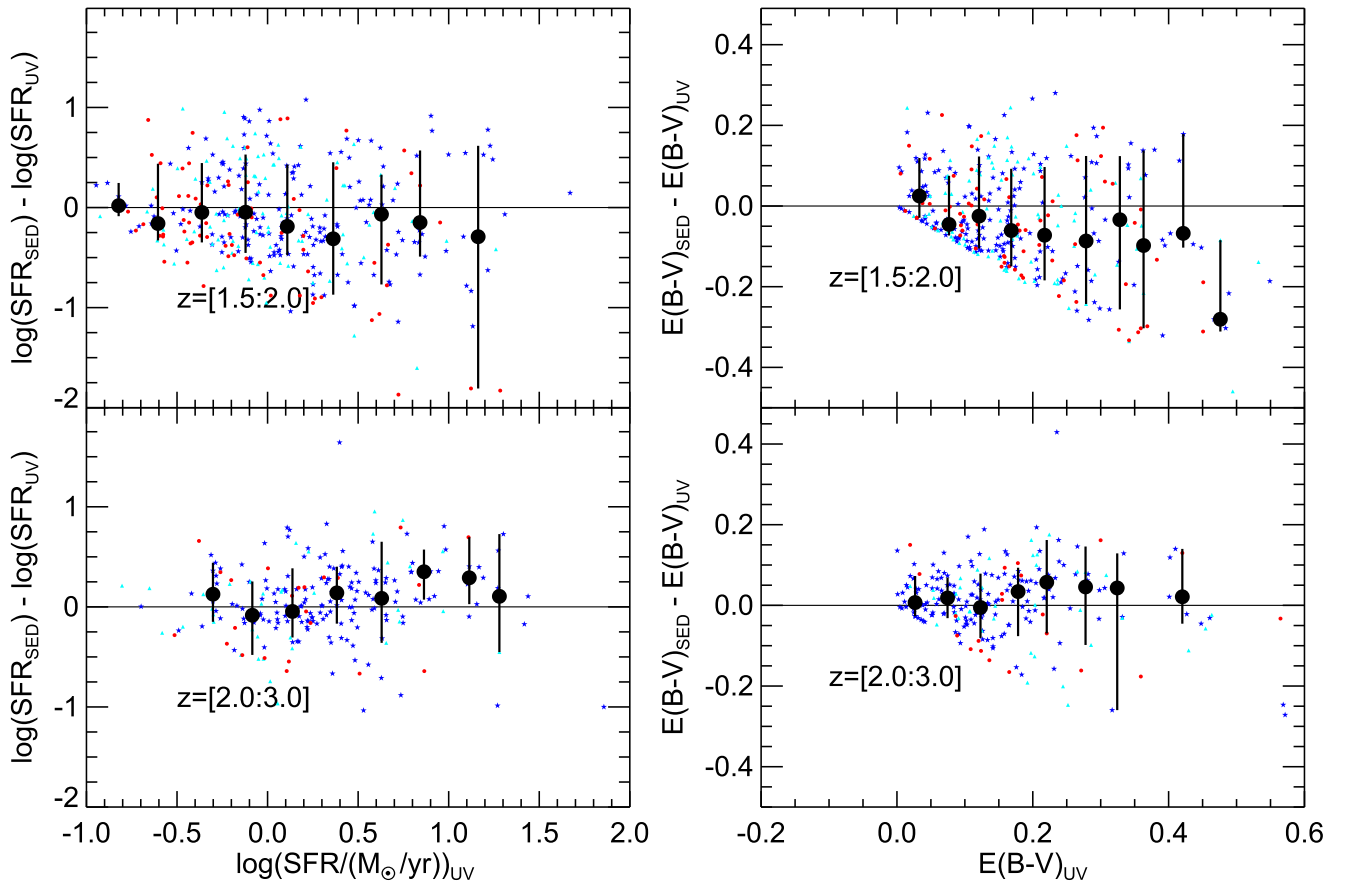
Figure 6. Comparisons of SFRs (left) and dust extinction $E(B − V)$s (right) measured through SED fitting and rest-frame UV continuum. The blue, cyan, and red data points are clumps with $f_{LUV} \equiv L_{clump}^{UV}/L_{galaxy}^{UV} > 0.08$, $0.05 < f_{LUV} < 0.08$, and $0.03 < f_{LUV} < 0.05$, respectively. Black circles with error bars show the median and 16th and 84th percentiles of the data. Clumps at $z \lesssim 1.5$ do not have enough *HST* filters to sample their rest-frame UV continuum and therefore are not shown in the figure.

gray contours. On average, when clumps' M_* is significantly lower than their host galaxies' M_*, the sSFR of clumps is about 5 times higher than the typical sSFR in galaxies with M_* similar to their host galaxies (i.e., compare massive clumps with contours within the two vertical dotted lines). This result is consistent with other studies (e.g., Guo et al. 2012b; Wuyts et al. 2012). The clear trend is for clumps' sSFR to increase with the decrease of M_*, with the most massive clumps having sSFR similar to that of their host galaxies. Very low-mass clumps' sSFR is up to 30 times higher than that of the host galaxies.

5.2. Radial Variation of Clump Color (Color Gradient)

Figure 8 shows the variation of the clump $U − V$ color as a function of galactocentric distance normalized by the SMA of their host galaxies (color gradient). The clump age gradient and sSFR gradient are usually used to test theoretical models of clump formation and evolution. These quantities, however, can only be derived through colors (SEDs) in our data set. Therefore, we first present the color gradient, because it is directly observed and the most robust result among all gradients discussed in this paper.

We find a color gradient in almost all panels at $z < 2$: clumps at small galactocentric distance (normalized by the SMA of their galaxies) are redder, while those at large distance are bluer. This result is similar to many other studies in the literature, e.g., Förster Schreiber et al. (2011), Guo et al.

(2012b), Tadaki et al. (2014), Shibuya et al. (2016), and Soto et al. (2017). At $z \geqslant 2$, clumps show almost no color gradients.

Our large data set covering wide ranges of redshift and M_* enables us to study the dependence of the color gradient on redshift and galaxy M_* for the first time. At the same galaxy M_*, the color gradient becomes steeper toward lower redshifts. Also, at the same redshift, the gradient becomes slightly steeper toward more massive galaxies.

We also calculate the color gradient of intra-clump regions (or diffuse background). To this purpose, we measure the multiband photometry of the host galaxies in circular annuli after masking the clump regions. We then use the same method as in Section 4 to derive the physical properties of intra-clump regions. Figure 8 shows that, overall, (1) intra-clump regions (brown lines in the figure) are redder than clumps and (2) the color gradient of intra-clump regions is flatter than that of clumps. In the lowest-M_* bin (10^9–$10^{9.8}\,M_\odot$), the intra-clump regions' color gradient is almost flat in all redshift bins. We also find marginal evidence (through a linear fit) that the slope of intra-clump regions' color gradient becomes steeper with galaxy M_* at $z \geqslant 1$. This result is consistent with recent studies of the color gradient of integrated light in galaxies, e.g., Liu et al. (2016), Tacchella et al. (2017), and Wang et al. (2017).

Figure 8 implies that clumps' color gradient at $z < 2$ would be changed if the colors were measured by using the fluxes without background subtraction. The color gradients of the diffuse background (brown solid lines) are significantly
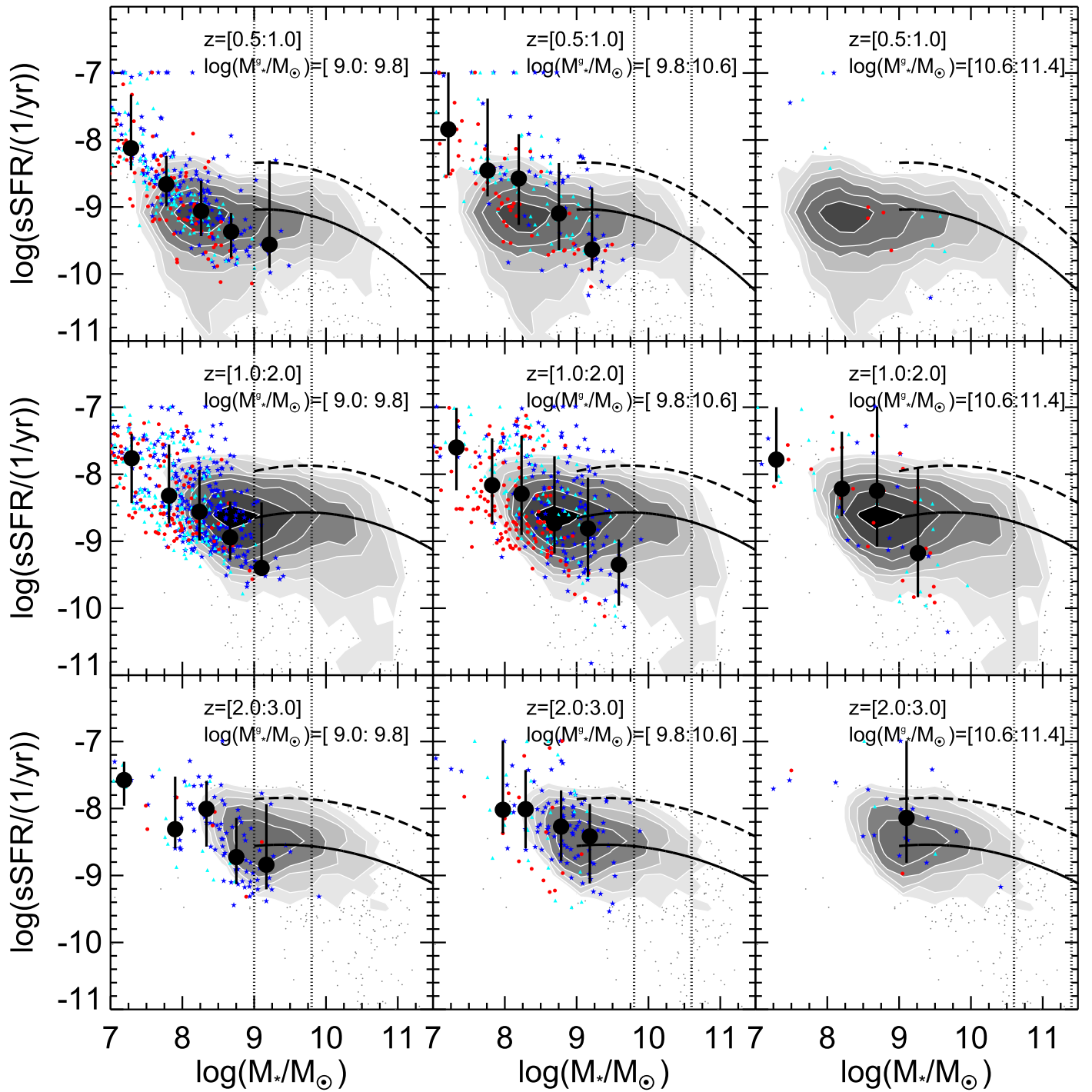
Figure 7. Similar to Figure 5 but showing the sSFR–M_* relation of clumps and integrated CANDELS/GOODS-S galaxies with F160W < 26 AB. Colored symbols, gray contours and points, and vertical dotted lines have the same meaning as in Figures 4 and 5. Black circles with error bars show the median and 16th and 84th percentiles of clump sSFRs in individual M_* bins. The solid black curves show the polynomial fit of the star formation sequence of Whitaker et al. (2014), and the dashed black lines are the solid lines scaled up by a factor of five.

different from that of clumps (large black circles): the former is almost flat, while the latter decreases with the normalized galactocentric distance. If the measurements without background subtraction are used, clumps would be redder than with background subtraction, with a big impact especially on the age–extinction determination. Moreover, without background subtraction, the clump color gradient would be flatter (see the top left panel of Figure 14 and more discussion in Section 5.7).

This result indicates that color gradients of clumps can only be made shallower—not the opposite—by the contribution of the diffuse background. It is hard to justify the observed color gradients in clumps as being introduced only by background contamination, which in the worst case would "dilute" those gradients. Therefore, the existence of a negative color gradient can be considered quite robust with respect to background contamination (or background-subtraction method).
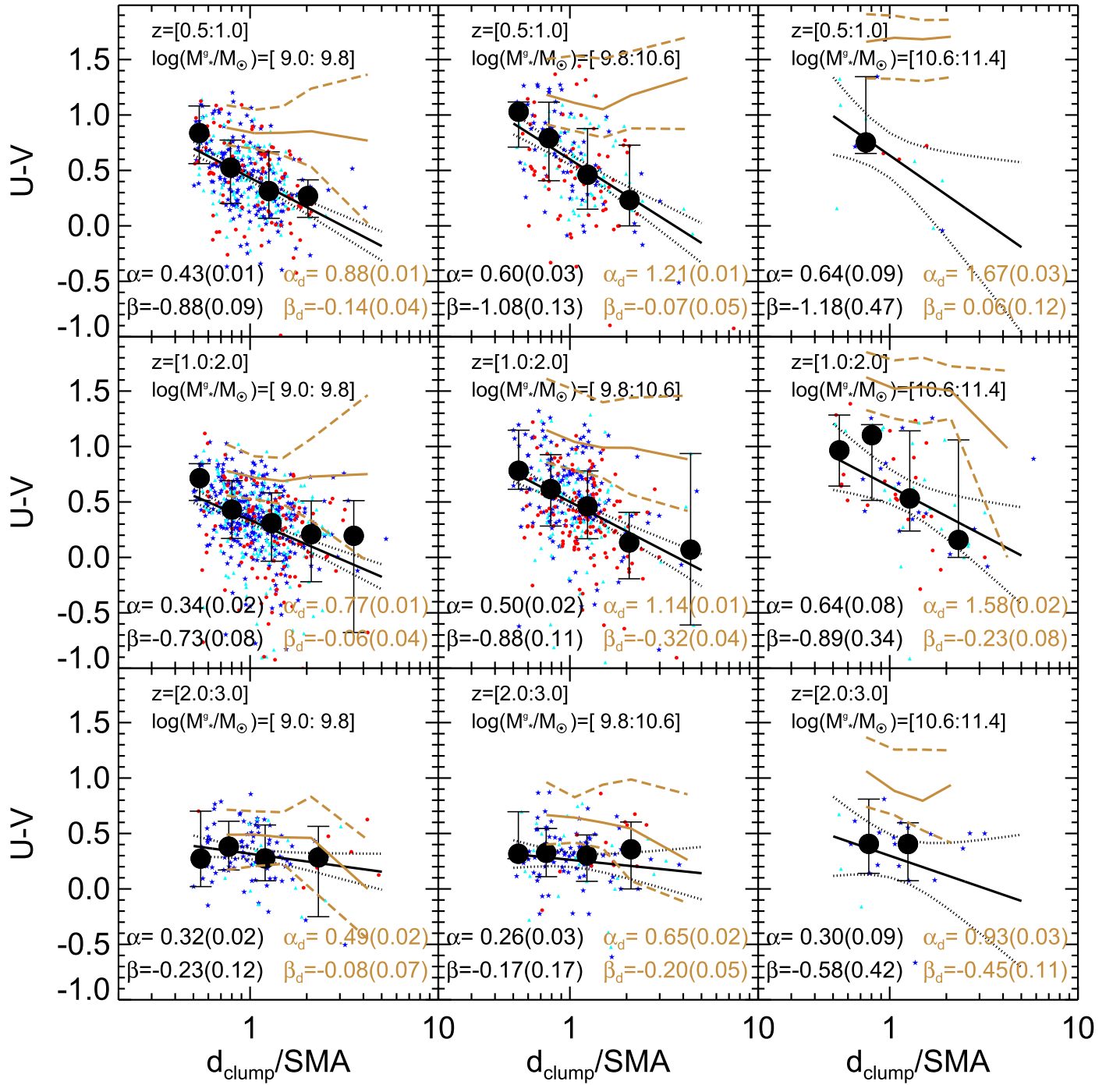
Figure 8. Variation of the rest-frame $U - V$ color of clumps as a function of their galactocentric distance normalized by SMA from host galaxy centers. Blue, cyan, and red points and black circles with error bars are the same as in Figures 4, 5, and 7. The galactocentric distance of clumps (d_{clump}) is scaled by the SMA of their galaxies. In each panel, the black solid line and dotted curves show the best linear fit (($U - V$) = $\alpha + \beta \log(d_{clump}/SMA)$) and its confidence level to the color points. The intersection (α) and slope (β) of each linear fit are shown in the lower left corner of each panel. The values within the parentheses are errors. Solid and dashed light brown curves in each panel show the median and deviation of the radial gradient of the $U - V$ color of intra-clump regions. The intersection (α_d) and slope (β_d) of the best linear fit to the diffuse component gradient are shown in the lower right corner.

On the other hand, since the individual clumps contribute only a few percent to the total UV light of their galaxies and even less to the M_* of the galaxies, the global color gradient of galaxies is actually dominated by the diffuse component, which is supported by the broad consistency between our measurement of the color gradient of the diffuse component and other measurements of the global color gradient in the literature.

The color gradient in Figure 8 is measured when the (projected) galactocentric distance is normalized by the SMA of the galaxies. We also use the physical projected galactocentric distance (in units of kpc) to measure the color gradient. Qualitatively, all of the above results are not changed. The slopes of the clump color gradient using the physical distance are actually steeper than those using the normalized distance, except in the lowest-mass bin at the highest redshift. We keep

using the normalized galactocentric distance for other gradients below.

Figure 8 also provides tests of the two selection effects discussed in Section 2.3: redshift-dependent and galaxy M_*-dependent biases, both introduced by our relative definition of clumps with a fixed f_{LUV} (i.e., at higher redshifts or higher galaxy M_*, only high f_{LUV} clumps are detected). For clumps in galaxies with $M_* < 10.8$ at $z < 2.0$ (where we have enough clumps), we recalculate the clump $U - V$ color gradient by dividing clumps into three subsamples: $0.03 \leqslant f_{LUV} < 0.05$, $0.05 \leqslant f_{LUV} < 0.08$, and $f_{LUV} \geqslant 0.08$. The three subsamples in each (z, M_*) bin show almost the same gradient, indicating that our results have almost no dependence on the adopted f_{LUV} thresholds. The comparison between different galaxy M_* bins at a given redshift is also robust with respect to the f_{LUV} threshold. For example, the result of the clump color gradient slopes increasing with galaxy M_* is still true even when we match the intrinsic luminosity of clumps in different galaxy M_* bins (e.g., by comparing low-f_{LUV} clumps from galaxies with $M_* > 9.8$ with high-f_{LUV} clumps from galaxies with $M_* \leqslant 9.8$). Overall, we conclude that our results of clump color gradient are not significantly affected by the selection effects.

5.3. Age Gradient

An important test of different clump evolution models is the age gradient. The inward migration scenario (e.g., Bournaud et al. 2007; Elmegreen et al. 2008; Ceverino et al. 2010; Bournaud et al. 2014; Mandelker et al. 2014) predicts a negative age gradient: inner (small galactocentric distance) clumps are older, while outer (large galactocentric distance) clumps are younger. In these models, clumps spend a few hundred Myr migrating from galaxy outskirts to galactic centers. Therefore, the age difference between inner and outer clumps should also be on the order of a few hundred Myr. Such a negative age gradient is found by some observations (e.g., Förster Schreiber et al. 2011; Guo et al. 2012b; Soto et al. 2017), consistent with the inward migration scenario. A few simulations, e.g., FIRE (Oklopčić et al. 2017) and NIHAO (Buck et al. 2017), however, argue that the age gradient may be a result of clumps being contaminated by old disk stars that happen to be in clump locations. Although these simulations are able to reproduce the trend of the observed clump age gradient, clump migration is not found in them. The clump ages in FIRE are significantly shorter—less than 50 Myr. In this paper, as discussed in Section 3, we try different diffuse background-subtraction configurations to statistically minimize the contamination of "disk" stars.

Figure 9 shows clump age as a function of clump galactocentric distance scaled by SMA. In our SED fitting, age is defined as the period from the onset of star formation (i.e., the beginning of the exponentially declining τ-model or constant SFH model) to the time the object is observed. The existence of a clump age gradient depends on the redshift and M_* of their host galaxies. We fit the relation $\log(age) = \alpha + \beta \times \log(d_{clump}/SMA)$ to our clump data and use β and its uncertainty (values are shown in the figure) to determine if an age gradient is significant. For galaxies with $M_* < 10^{10.6} M_\odot$ and $z < 2.0$, β is smaller than zero by more than 3σ. We therefore conclude an existence of clump age gradients for these galaxies. For galaxies at $z \geqslant 2.0$, β is consistent with zero within $\sim 1\sigma$, indicating a flat age distribution with galactocentric distance, namely, no gradient. For very massive

($M_* \geqslant 10^{10.6} M_\odot$) galaxies at $z < 2.0$, β deviates from zero by about 2σ, showing a marginal age gradient. Given the small-number statistics of very massive galaxies, no firm conclusion can be drawn from our data set for them. Future studies of larger samples are needed.

Using the best-fit relation, we can calculate the age difference between inner and outer clumps. We use $d_{clump}/SMA = 0.5$ as the typical location of inner clumps. At a distance smaller than this, we cannot separate clumps from galactic bulges due to the resolution of HST images (see Paper I for related discussions). For outskirts, we use $d_{clump}/SMA = 2.0$ as the typical location of the outer clumps. This choice is motivated by the fact that, for star-forming galaxies with Sérsic index $n = 1$, the disk size is about $2\times$ SMA. For galaxies with $M_* < 10^{10.6} M_\odot$ and $z < 1.0$, the age difference between $d_{clump}/SMA = 0.5$ and 2.0 is about 700 Myr, while for galaxies with $M_* < 10^{10.6} M_\odot$ and $1.0 \leqslant z < 2.0$, the age difference is about 250–300 Myr.

We also compare clump age gradients with the age gradients of the diffuse background (brown lines and values in the figure). The diffuse background properties are measured from the annulus photometry as described in Section 5.2. We use the same SED-fitting procedure to derive the properties, e.g., age, M_*, SFR, $E(B - V)$, etc. Here we compare the slopes of the best-fit gradients (β for clumps and β_d for diffuse background in the figure). At $M_* < 10^{10.6} M_\odot$ and $z < 2.0$, where we find obvious ($>3\sigma$) clump age gradients, the clump age gradient is significantly steeper than the diffuse background's age gradient. In fact, the diffuse background only shows an obvious ($>3\sigma$) age gradient for low-mass galaxies with $M_* < 10^{9.8} M_\odot$. Moreover, at $z < 2.0$, the age of inner clumps ($d_{clump}/SMA < 0.5$) is older than that of the inner part of the diffuse background.

In our SED fitting, the lower limit of the age of the stellar population models is 10 Myr (see Table 3). Using younger models in our SED-fitting procedure would result in an unphysically high SFR for some clumps. As a result of the age limit, a small fraction of clumps are stalled at $\log(age/Gyr) \sim -2$ (more obviously seen in the two panels of $0.5 \leqslant z < 1.0$ and $M_* < 10^{10.6} M_\odot$). For these clumps, we likely over-estimate their ages. This caveat, however, does not significantly bias our age-gradient measurement, because the number of these possibly very young clumps is small. In observation, so far only one clump (Zanella et al. 2015) was measured to be younger than 10 Myr. Although some simulations, e.g., FIRE, predict very short-lived clumps, our lower age limit is still younger than the mean lifetime of their massive clumps (~ 20 Myr; Oklopčić et al. 2017), giving our measurements enough diagnostic power to test their models.

5.4. Dust Extinction Gradient

Figure 10 shows the radial variation of clump dust extinction, $E(B - V)$, as a function of galactocentric distance. Overall, clumps show a negative $E(B - V)$ gradient: inner clumps are more dust-extincted, while outer clumps have little extinction. The slopes of the clump $E(B - V)$ gradients depend on galaxy M_*: at a given redshift, the gradient becomes steeper as galaxy M_* increases. For a given galaxy M_*, however, the gradient shows no obvious dependence on redshift.

Because of the age–dust degeneracy, the observed clump $U - V$ color gradient (Figure 8) can be explained by an age
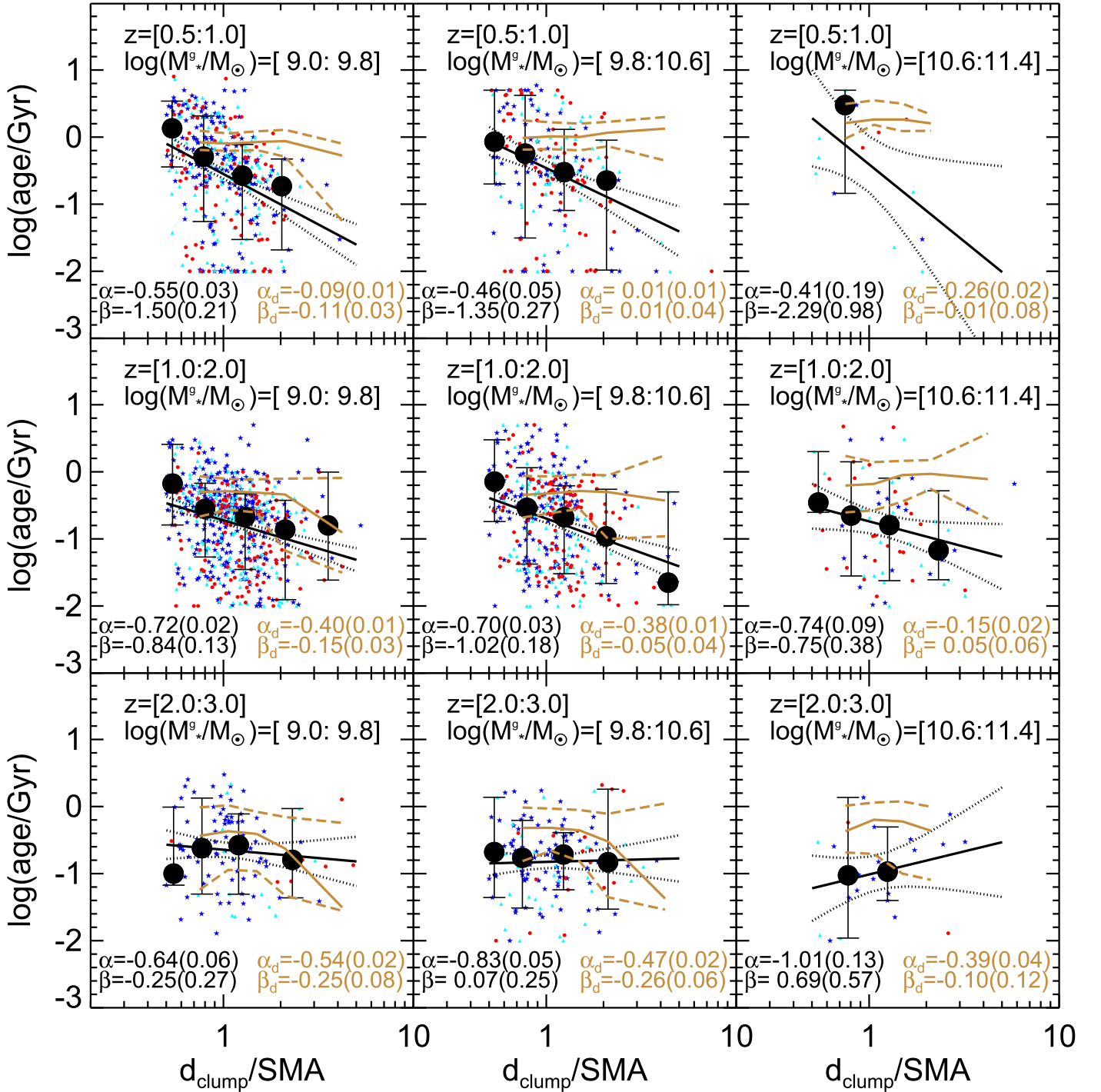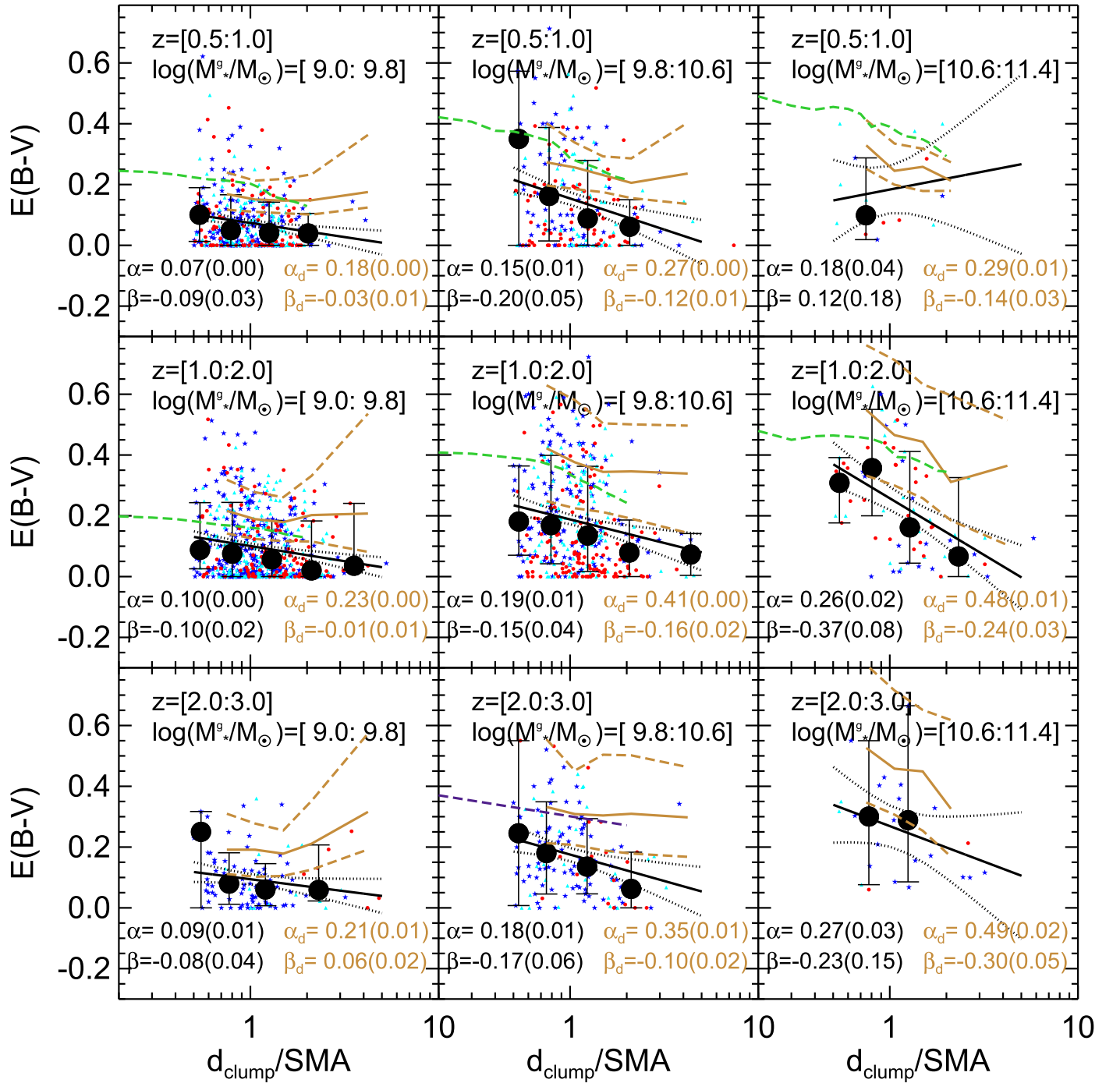
Figure 9. Similar to Figure 8, but for the radial gradient of the age of clumps.

gradient, an extinction gradient, or a combination of both. Our SED fitting measures age and $E(B - V)$ simultaneously and attributes the observed $U - V$ gradient to both age (Figure 9) and $E(B - V)$ (Figure 10). If there was no age gradient as shown in Figure 9, the $E(B - V)$ gradient would be much stronger, and vice versa.

One way to test our SED-fitting procedure is to study the $E(B - V)$ gradient of the diffuse component and compare it with the literature. Diffuse background and clumps have similar slopes for the $E(B - V)$ gradients, but clumps are systematically less dust-extincted. This result is not surprising,

because clumps are selected as UV-bright regions and hence are likely to have less dust extinction.

We compare our measurements (brown lines in Figure 10) with those of Wang et al. (2017; green dashed lines) and Tacchella et al. (2017; purple dashed line). The methods used by Wang et al. and Tacchella et al. are different from ours. Wang et al. calibrated the relation between $E(B - V)$ (and sSFR) and colors in the rest-frame UVI diagram (a substitute of the UVJ diagram) of integrated galaxies and applied the calibrations to multiwavelength multi-aperture photometry. Tacchella et al. used the rest-frame UV continuum to measure

Figure 10. Similar to Figure 9, but for the radial gradient of dust extinction, $E(B - V)$, of clumps. Green and purple dashed lines show the $E(B - V)$ profiles measured by Wang et al. (2017) and Tacchella et al. (2017).

$E(B - V)$ and sSFR for massive galaxies at $z \sim 2.2$. Both Wang et al. and Tacchella et al. used all pixels to measure the profiles, while we only use intra-clump pixels (i.e., those not masked as clump locations; see the white pixels in the bottom right panel of Figure 2). This difference may result in different slopes of the $E(B - V)$ profiles in our and their studies. In this test, however, we only focus on the absolute values within the galactocentric ranges covered by both our and other studies (i.e., between 0.5 and 2 SMA).

The measurements of the two groups, although derived by different methods, show good agreement with our results. The

difference between their and our $E(B - V)$ profiles is within the scatter of our measurements, except for the most massive bin at $z < 1.0$, where both our and Wang et al.'s samples suffer from small-number statistics.

Overall, this result demonstrates that our SED-fitting procedure induces no significant systematics compared with other studies. When breaking the age–dust degeneracy, our method yields consistent results with similar studies in the literature. Based on our results, we argue that to explain the observed clump $U - V$ gradient requires both an age gradient and an $E(B - V)$ gradient simultaneously. Liu et al. (2016) also
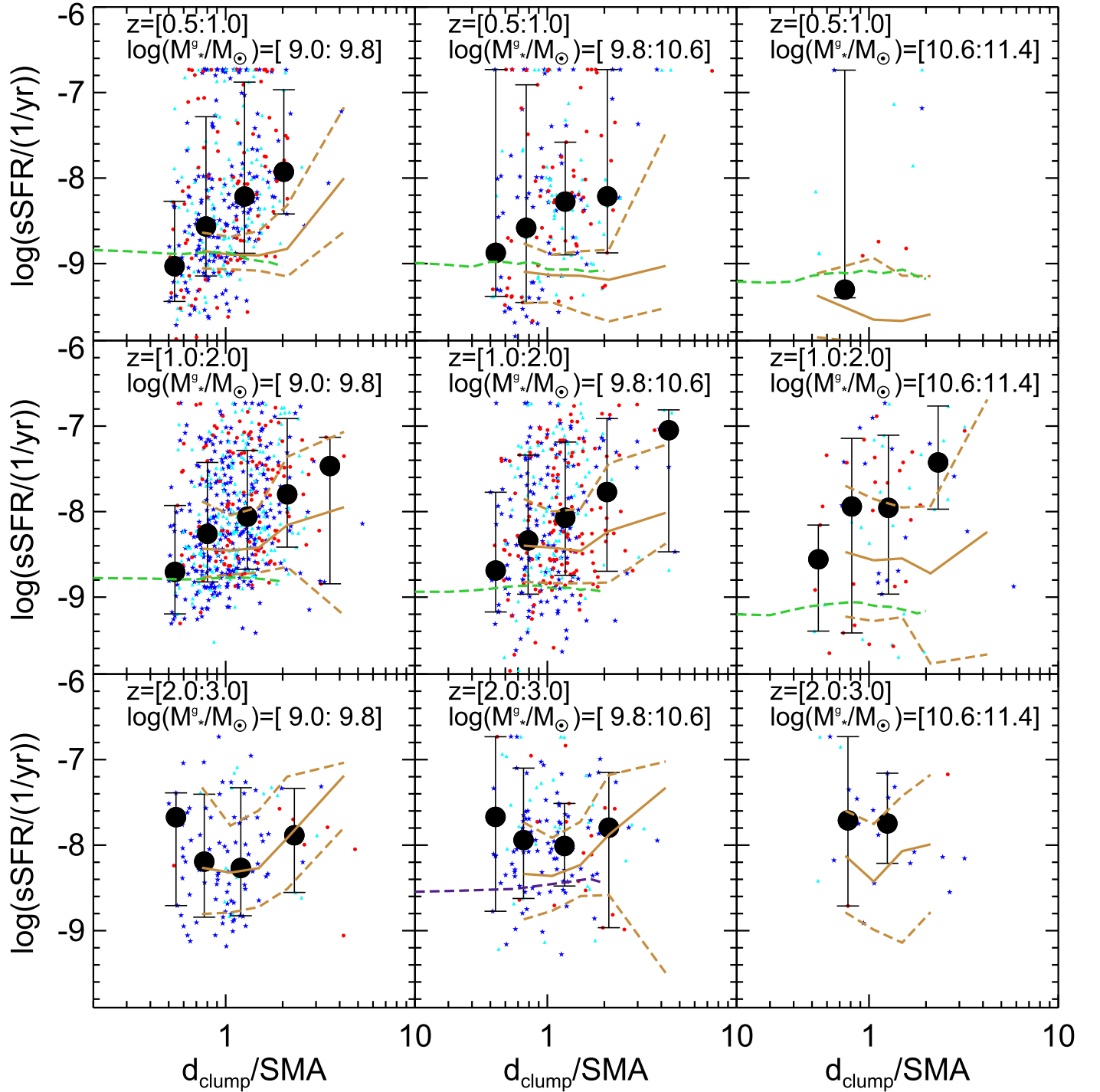
Figure 11. Similar to Figure 10, but for the radial gradient of the sSFR of clumps and diffuse background.

showed that the observed color gradient of galaxies is composite with both stellar population and $E(B-V)$ gradients.

An additional method to assess the simultaneous need of both age and dust extinction gradient is to "marginalize" over either age or $E(B-V)$. In this method, we assume no radial gradient for one quantity and use the other one to explain the observed UV color gradients of clumps. This method requires clumps near galactic centers to be unrealistically old/dusty.

We use clumps in galaxies with $9.8 \leqslant \log(M_*/M_\odot) < 10.6$ at $1.0 \leqslant z < 2.0$ as an example. The UV colors of these clumps drop from $U-V \sim 0.8$ at near galactic centers to ~ 0

at $\sim 3\times$ SMA. If we fix $E(B-V) = 0.0$ for all radii and assume a constant SFH, the inner clumps need to be as old as ~ 5 Gyr to reach $U-V \sim 0.8$, which is older than the age of the universe at $z \sim 1.5$. If we choose a τ-model with $\tau = 0.5$ Gyr for the SFH, the inner clumps would have an age of 1 Gyr. This age is younger than the age of the universe but still two times older than the characteristic timescale of SF, suggesting the clump SF is being quenched, which is inconsistent with the prominent UV luminosity of the clumps.

On the other hand, if we fix the clump age as 30 Myr across all radii, the inner clumps need to have $E(B-V) \sim 0.5$ to
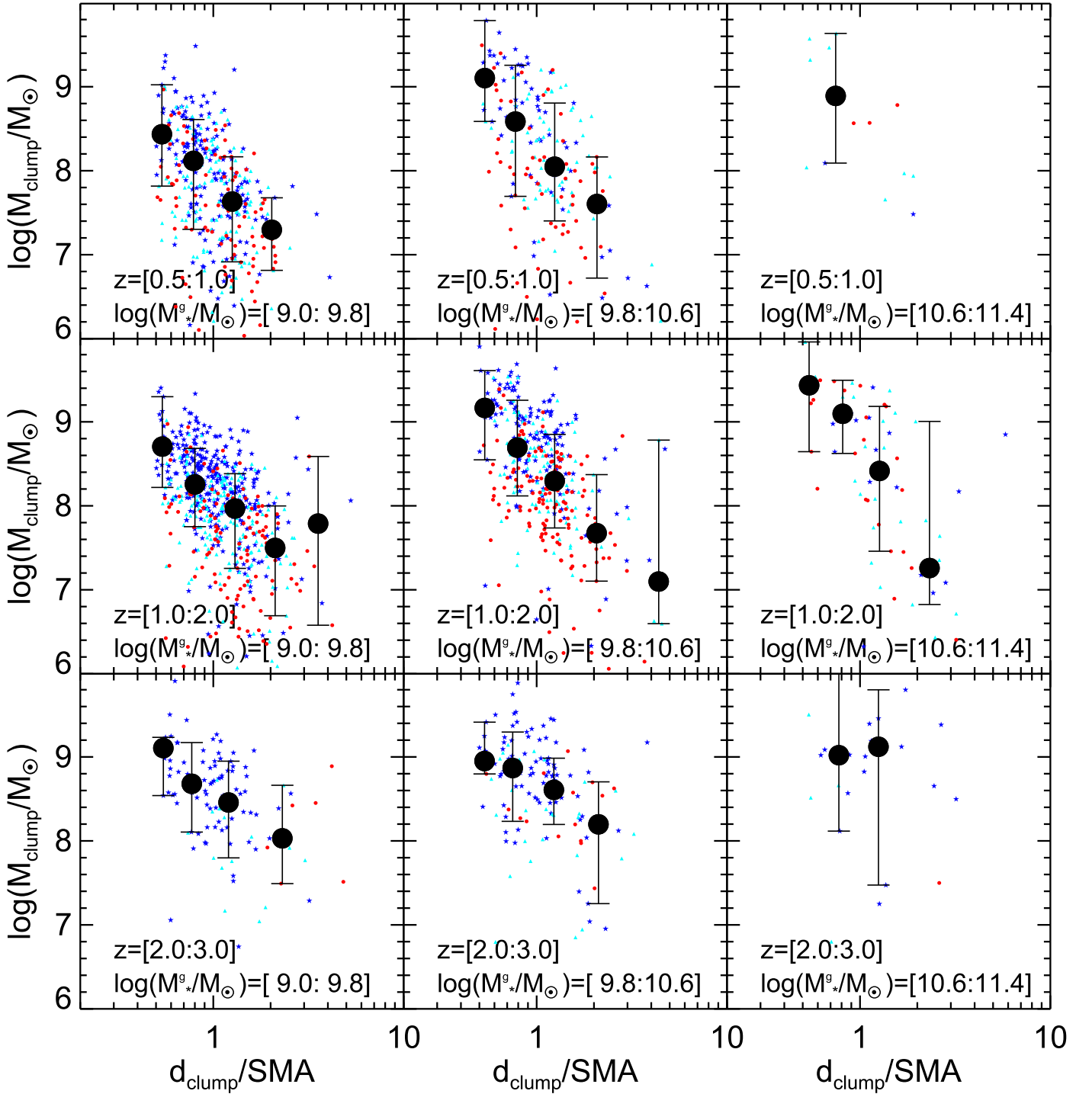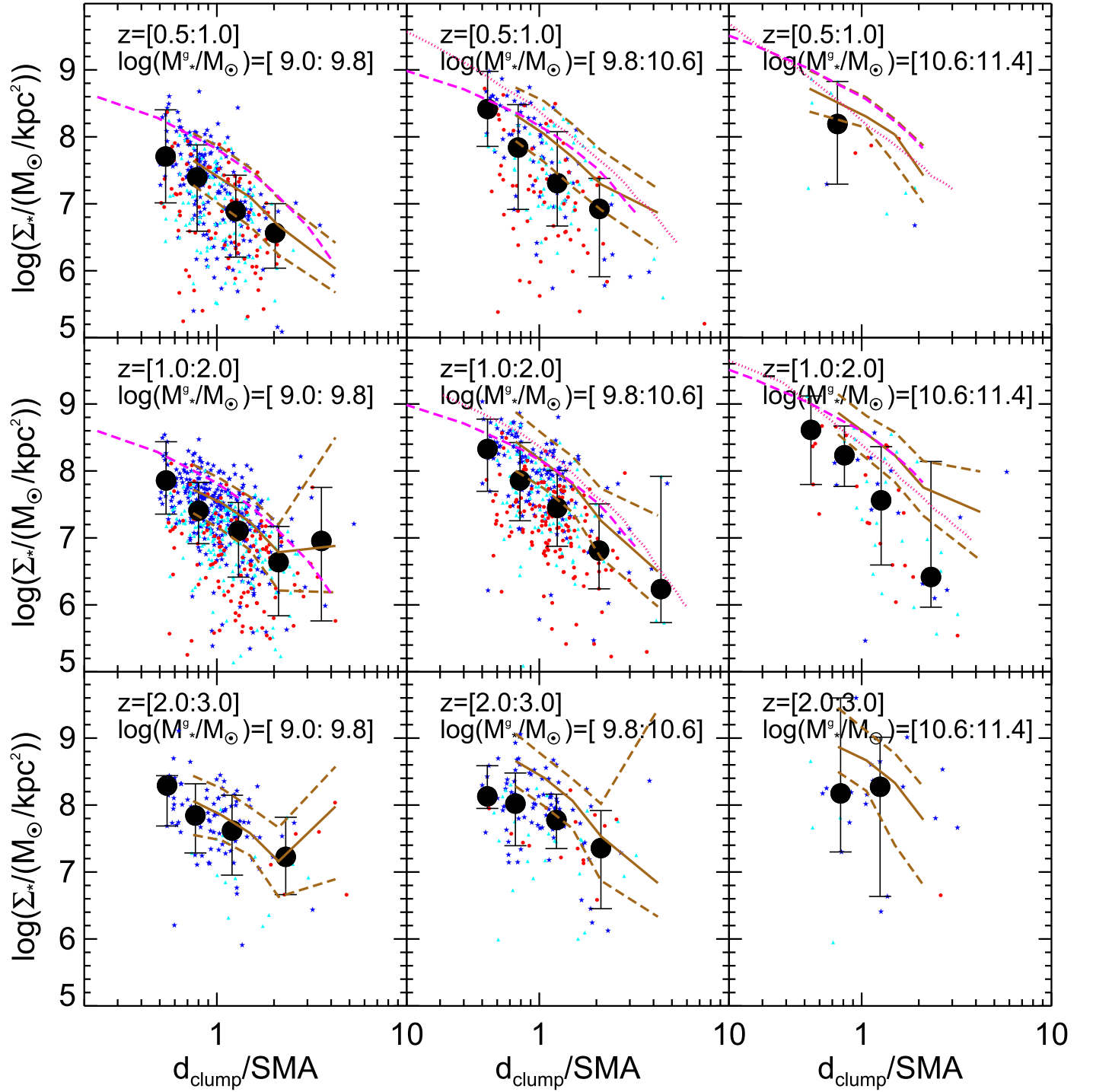
Figure 12. Similar to Figure 9, but for the radial gradient of M_* of clumps.

reach $U - V \sim 0.8$. According to the Calzetti extinction law adopted in our paper, $A_{NUV(2800A)}$ of the inner clumps would therefore be 3.6 mag, resulting in the dust-corrected NUV luminosity of inner clumps being ~30 times brighter than what we observed. With such high attenuation, even a single clump (considering each contributing 5% of the "observed" UV luminosity of the galaxy) would easily have an SFR larger than the global SFR of the total galaxy. Therefore, we believe that dust extinction alone cannot fully explain the observed clump $U - V$ gradient. This test of $E(B - V)$ has little dependence on the choice of clump age and SFH.

5.5. sSFR Gradient

Figure 11 shows the sSFR gradient of clumps. At $z < 2.0$ (except for the most massive galaxies, $10^{10.6} M_\odot < M_* < 10^{11.4} M_\odot$, at $0.5 \leqslant z < 1.0$, where the sample size is tiny), clumps exhibit strong radial variation: the sSFR of inner clumps (at $d_{clump}/SMA = 0.5$) is about 1 dex lower than that of outer clumps (at $d_{clump}/SMA \gtrsim 0.5$).

Similar to the test of the dust extinction gradient, we also measure the sSFR gradients of the diffuse background (brown lines) and compare our results with those of Wang et al. (2017;

19

Figure 13. Similar to Figure 9, but for the radial gradient of M_* surface density of clumps. Magenta dashed lines and pink dotted lines show the profiles measured by Nelson et al. (2016a) and Mosleh et al. (2017), respectively.

green dashed lines) and Tacchella et al. (2017; purple dashed line). Our results show excellent agreement with these studies at $z < 1.0$ and $z \geqslant 2.0$. At $1.0 \leqslant z < 2.0$, however, our measurements are higher, although still within the uncertainties, than those of Wang et al. A possible reason is the redshift distributions: the sample of Wang et al. is in fact at $z < 1.4$, while our sample covers the whole redshift range of $1.0 \leqslant z < 2.0$. The lack of $z > 1.4$ (and more actively star-forming) galaxies in Wang et al. therefore biases their measurement to lower values compared to our sample. Overall,

good agreement between our and other studies ensures the accuracy of our sSFR gradient measurement.

Our results, together with those of Wang et al. and Tacchella et al., show that the diffuse background (or integrated) sSFR gradient (or sSFR profile) is almost flat from the galactic center to $2 \times$ SMA. Beyond $2 \times$ SMA, our results show marginal evidence of an increasing sSFR toward large galactocentric distance. At $z < 2.0$, the clump sSFR gradient is steeper than that of the diffuse component: inner clumps have similar or even lower sSFR than the diffuse background, while outer
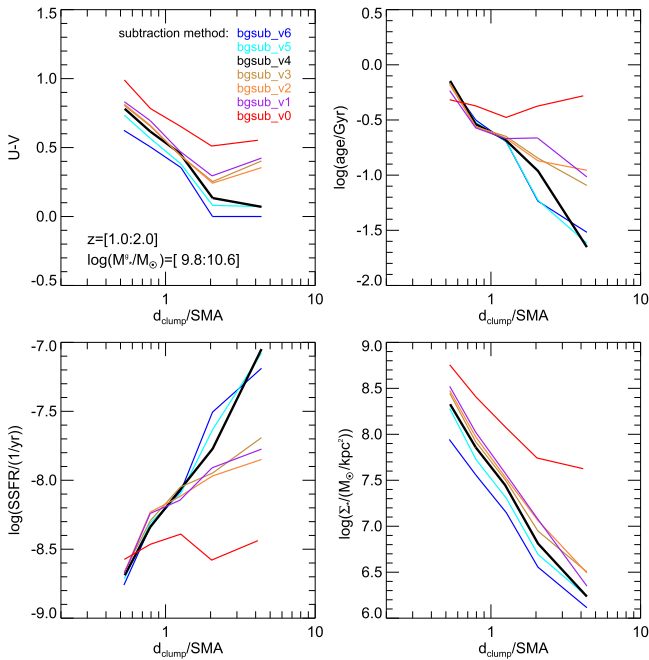
Figure 14. Effects of different diffuse background subtractions. As an example, we show the gradients of rest-frame $U - V$ color, age, sSFR, and M_* surface density of clumps in galaxies with $1.0 < z < 2.0$ and $10^{9.8}\,M_\odot < M_* < 10^{10.6}\,M_\odot$. Different colored lines show the median relations with different diffuse background-subtraction methods as indicated by the labels (see Table 2 for details). Our fiducial subtraction method (bgsub_v4) is shown by the black lines.

clumps' sSFR is about ∼0.5 dex higher than that of the background.

5.6. Stellar Mass and Stellar Mass Density Gradients

Figure 12 shows the radial variation of M_* of clumps. In all redshift and galaxy M_* bins where the sample size is large enough, clumps show a significant M_* gradient: inner clumps are on average more massive than outer clumps by a factor of a few tens to hundred.

Figure 13 shows the radial variation of the stellar mass density (Σ_*) of clumps. Here Σ_* is calculated within a circle with a radius of $0''\!.18$ (3 pixels), namely, the aperture size that is used to measure the clump photometry. Clumps show a significant Σ_* gradient in almost all redshift and galaxy M_* bins (except for the two most massive bins with small sample statistics): inner clumps are on average denser than outer clumps by a factor of ∼10–30.

In fact, the Σ_* measured above should be treated as the lower limit of the true clump Σ_*. In this paper, we assume clumps are unresolved sources and use $0''\!.18$ as their radius. This choice is comparable to the FWHM of *HST* F160W, below which sources are unresolved. The actual size of clumps is uncertain, ranging from ∼100 pc to ∼1 kpc. Our aperture of $0''\!.18$ is equal to ∼1.5 kpc at $z \sim 1$, which is much larger than most clump size measurements in the literature. Our clump size is therefore an upper limit of the size of an unresolved source. Accordingly, the measured Σ_* is a lower limit. Moreover, the Σ_* gradient will only be true if clump size has no dependence on galactocentric distance.

We also show Σ_* profiles of diffuse components from our sample (brown lines in the figure) and from Nelson et al. (2016a; magenta dashed lines) and Mosleh et al. (2017; pink

dotted lines). Nelson et al. (2016a) converted the observed F140W light profile into a mass surface density profile by applying the integrated M_*-to-F140W ratio as a constant scale factor at all radii. Mosleh et al. (2017) used FAST (Kriek et al. 2009) to measure M_* at each radius. Both Nelson et al. (2016a) and Mosleh et al. (2017) provided Σ_* profiles in units of kpc. We scaled their galactocentric distance by the average size of galaxies in their samples in each redshift and M_* bin. Overall, the agreement is good: the difference between our and their studies is within the confidence level of our measurements. The slopes of the profiles differ from one study to another. As we discuss in the comparison of $E(B - V)$ profiles, we only focus on the absolute values rather than the slopes to test any significant systematics. Given this purpose, the encouraging comparison results support the accuracy of our measurement.

On average, clump Σ_* is a few times lower than that of the diffuse background at the same galactocentric distance. Wuyts et al. (2012) studied the Σ_* of clump pixels in massive galaxies at $0.5 \leqslant z < 2.5$ and found that when clumps are detected from the rest-frame U band, the Σ_* of clump pixels is about 10 times smaller than the Σ_* of diffuse background at the half-light radius determined in the U band. Our results are broadly consistent with those of Wuyts et al. (2012).

The above result is apparently surprising, as one may expect that clumps are on average denser than the diffuse component, because clumps represent star-forming regions and, given their estimated ages (tens to hundreds of Myr), are expected to be dominated by stars. A few factors are contributing to this result. First and most importantly, as discussed above, the clump Σ_* measurement should be treated as a lower limit. Our aperture of $0''\!.18$ is actually an upper limit of clump size. This value corresponds to about 1.5 kpc at $z \sim 1$. If the intrinsic clump size is 500 pc (some authors even argue for smaller ones), the clump mass surface density is underestimated by a factor of nine with our aperture size. Second, our fiducial background subtraction reduces the clump mass by a factor of two compared to the case of no subtraction.

5.7. Effects of Diffuse Background Subtraction

All gradients present in this section are based on our fiducial diffuse background subtraction (bgsub_v4 in Table 2 and Section 3). Different subtractions would result in different gradients. It is important to test if the gradients observed in this section are robust to different subtraction methods. Particularly, it is interesting to test if changing the background subtraction would make the age gradient flat. As argued by Buck et al. (2017) and Oklopčić et al. (2017), the negative clump age gradient (inner old, outer young) may be a result of clumps being contaminated by disk stars. To test the robustness, we repeat all previous measurements with different background-subtraction methods in Table 2. Here we only use one redshift and galaxy M_* bin ($1.0 < z < 2.0$ and $10^{9.8}\,M_\odot < M_* < 10^{10.6}\,M_\odot$) to illustrate the effects. This bin is representative and may be of interest to many readers.

The test results are shown in Figure 14. For the $U - V$ color, the overall trend of color gradient is preserved from very aggressive subtraction (bgsub_v6; blue) to no subtraction (bgsub_v0; red), although the clump colors become redder gradually from bgsub_v6 to bgsub_v0. This is expected because background stars are older than clump stars

Table 4
Clump Catalog Columns

Column	Name	Note	Reference
Part I: Galaxy Properties			
1	Galaxy ID	CANDELS ID	Guo et al. (2013)
2	R.A.	J2000	⋯
3	Decl.	J2000	⋯
4	Redshift		Dahlen et al. (2013)
5	M_*	log $M_\odot$	Mobasher et al. (2015); Santini et al. (2015)
6	M_* error	dex	⋯
7	SFR	log $(M_\odot\ \mathrm{yr}^{-1})$	⋯
8	SFR error	dex	⋯
9	Rest-frame U	mag	Kocevski et al. (2017)
10	Rest-frame V	mag	⋯
11	Rest-frame J	mag	⋯
12	SMA	arcsec	van der Wel et al. (2014)
13	SMA error	arcsec	⋯
Part II: Observed Clump Properties			
14	Clump ID		Guo et al. (2015)
15	Clump R.A.	J2000	⋯
16	Clump decl.	J2000	⋯
17	Clump detection band		Guo et al. (2015) or Section 2.2
18	Clump f_{LUV}		Guo et al. (2015)
19	Background-subtraction configuration		Section 3.1; Table 2
20, 21	F435W flux and error	μJy	Section 3
22, 23	F606W flux and error	μJy	⋯
24, 25	F775W flux and error	μJy	⋯
26, 27	F814W flux and error	μJy	⋯
28, 29	F850LP flux and error	μJy	⋯
30, 31	F105W flux and error	μJy	⋯
32, 33	F125W flux and error	μJy	⋯
34, 35	F140W flux and error	μJy	⋯
36, 37	F160W flux and error	μJy	⋯
38	Galactocentric distance	normalized by galaxy SMA	Guo et al. (2015)
Part III: Derived Clump Properties			
39	Clump photo-z		Section 3.2
40	*badczflag*		Section 3.2
41, 42, 43	M_* and its lower and upper 1σ	log $M_\odot$	Section 4.1
44, 45, 46	SFR and its lower and upper 1σ	$\log(M_\odot\ \mathrm{yr}^{-1})$	⋯
47, 48, 49	$E(B-V)$ and its lower and upper 1σ		⋯
50, 51, 52	Age and its lower and upper 1σ	log(Gyr)	⋯
53, 54, 55	τ and its lower and upper 1σ	log(Gyr)	⋯
56, 57	Rest-frame U and error	mag	⋯
58, 59	Rest-frame B and error	mag	⋯
60, 61	Rest-frame V and error	mag	⋯
62, 63	UV SFR and error	$\log(M_\odot\ \mathrm{yr}^{-1})$, dex	Section 4.4
64, 65	UV $E(B-V)$ and error		⋯
66	*veryredflag*		Section 4.3
67	*badmassflag*		Section 6
68	*extremesfrflag*		⋯

(Figure 8), and adding diffuse background light to clumps makes the latter redder. Moreover, the panel shows that outer clumps are affected by background subtraction more than inner clumps are.

Age and sSFR gradients are significantly affected by background subtraction. From very aggressive subtraction (bgsub_v6; blue) to very conservative subtraction (bgsub_v1; purple), both gradients become flatter. Eventually, when no background subtraction is applied (bgsub_v0; red), both gradients become flat. This change is again mostly driven by the effects of outer clumps. From bgsub_v6 to bgsub_v1, the

age (sSFR) of clumps at $4 \times d_{\mathrm{clump}}$/SMA becomes older (smaller) by a factor of three (six). Inner clumps, however, are hardly changed in various subtractions. For example, in most of the subtraction methods, the sSFR and age of the clumps with a galactocentric distance smaller than SMA are little changed.

The M_* surface density is similar to the $U - V$ color: the overall trend is preserved, but the amplitude changes. From bgsub_v1 (purple) to bgsub_v6 (blue), Σ_* decreases by a factor of three, because more and more light is subtracted from clumps. No subtraction (bgsub_v0; red) is even denser than aggressive subtraction (bgsub_v6; blue) by another factor of

three, approaching the Σ_* profile of the diffuse background (brown, magenta, and pink lines in the middle panel of Figure 13).

Overall, we conclude that background-subtraction methods (except for the no-subtraction one) would not change our conclusions on the existence of the $U - V$, age, sSFR, and Σ_* gradients of clumps, although they may alter the amplitude and slope of each gradient. Also, outer clumps are more vulnerable to background subtraction than inner clumps are.

6. Catalog Release and Use

We release the clump catalogs with the electronic version of this paper. The columns of the catalog are described in Table 4. We release the clump parameters measured with all background-subtraction methods in Table 2. In the released catalog, Columns 19–68 are repeated for each background-subtraction method (the method is given by Column 18).

We also suggest that readers apply the following criteria to exclude clumps with problematic photometry or derived properties.

1. *badczflag* = 1. These clumps have catastrophic photo-*z*s compared with the redshifts of their galaxies, which implies photometric errors (see Section 3.2).
2. *veryredflag* = 1. These clumps have rest-frame $U - V$ colors redder than the separation of the blue cloud and red sequence of integrated galaxies, which also indicates a photometry problem (see Section 4.3).
3. *badmassflag* = 1. These clumps' M_* is larger than that of their host galaxies, indicating an error in either photometry or SED fitting (see Section 4.5).
4. *extremesfrflag* = 1. These clumps' $\log(\mathrm{SFR}/(M_\odot\,\mathrm{yr}^{-1}))$ is larger than 3 or smaller than -2, indicating that the SED fitting chooses an extreme solution, possibly due to an error in either photometry or SED fitting.

7. Summary

As a step to establish a benchmark of direct comparisons of clumps between observations and theoretical models, we present a sample of clumps that, to the best of our knowledge, represents the commonly observed non-lensed "clumps" discussed in the literature. This sample contains 3193 clumps detected from 1270 galaxies at $0.5 \leqslant z < 3.0$. The clumps are detected from rest-frame UV images as described in Paper I. The physical properties of the clumps (e.g., rest-frame color, M_*, SFR, age, and dust extinction) are measured through fitting clump SEDs to synthetic stellar population models.

We carefully test the procedures of measuring clump properties in a few ways: (1) clump M/L, (2) clump color–M_* diagram, (3) SFRs and $E(B - V)$s measured by both SED fitting and UV continuum, and (4) as an indirect test, comparisons between our and others' measurements of the radial profiles of physical properties. We also test the effects of subtracting background fluxes from the diffuse component (or intra-clump regions) of galaxies on the observed clump gradients.

We show some examples of the measured physical properties. We find that clumps show radial $U - V$ color variation: clumps close to galactic centers are redder than those in outskirts. The slope of the color gradient (clump color as a function of the galactocentric distance scaled by the SMA of

galaxies) changes with redshift and stellar mass of the host galaxies: at a fixed stellar mass, it becomes steeper toward low redshift; and at a fixed redshift, it becomes steeper toward massive galaxies. Based on our SED fitting, this observed color gradient can be explained by a combination of a negative age gradient, a negative $E(B - V)$ gradient, and a positive sSFR gradient of clumps. The color gradients of clumps are steeper than those of intra-clump regions ("disks"). Correspondingly, the radial gradients of the derived physical properties of clumps are different from those of the diffuse component (intra-clump regions or "disks").

ORCID iDs

Yicheng Guo ◉ https://orcid.org/0000-0003-2775-2002
Marc Rafelski ◉ https://orcid.org/0000-0002-9946-4731
Eric F. Bell ◉ https://orcid.org/0000-0002-5564-9873
Christopher J. Conselice ◉ https://orcid.org/0000-0003-1949-7638
Avishai Dekel ◉ https://orcid.org/0000-0003-4174-0374
Mauro Giavalisco ◉ https://orcid.org/0000-0002-7831-8751
Anton M. Koekemoer ◉ https://orcid.org/0000-0002-6610-2048
David C. Koo ◉ https://orcid.org/0000-0003-3385-6799
Yu Lu ◉ https://orcid.org/0000-0003-2691-1622
Nir Mandelker ◉ https://orcid.org/0000-0001-8057-5880
Joel R. Primack ◉ https://orcid.org/0000-0001-5091-5098
Daniel Ceverino ◉ https://orcid.org/0000-0002-8680-248X
Duilia F. de Mello ◉ https://orcid.org/0000-0003-1624-8425
Henry C. Ferguson ◉ https://orcid.org/0000-0001-7113-2738
Nimish Hathi ◉ https://orcid.org/0000-0001-6145-5090
Ray Lucas ◉ https://orcid.org/0000-0003-1581-7825
Emmaris Soto ◉ https://orcid.org/0000-0002-2390-0584

References

Barro, G., Faber, S. M., Koo, D. C., et al. 2017, ApJ, 840, 47
Barro, G., Kriek, M., Pérez-González, P. G., et al. 2016, ApJL, 827, L32
Bassett, R., Glazebrook, K., Fisher, D. B., et al. 2014, MNRAS, 442, 3206
Boada, S., Tilvi, V., Papovich, C., et al. 2015, ApJ, 803, 104
Borch, A., Meisenheimer, K., Bell, E. F., et al. 2006, A&A, 453, 869
Bournaud, F., Daddi, E., Elmegreen, B. G., et al. 2008, A&A, 486, 741
Bournaud, F., Daddi, E., Weiß, A., et al. 2015, A&A, 575, A56
Bournaud, F., Dekel, A., Teyssier, R., et al. 2011, ApJL, 741, L33
Bournaud, F., Elmegreen, B. G., & Elmegreen, D. M. 2007, ApJ, 670, 237
Bournaud, F., Elmegreen, B. G., & Martig, M. 2009, ApJL, 707, L1
Bournaud, F., Juneau, S., Le Floc'h, E., et al. 2012, ApJ, 757, 81
Bournaud, F., Perret, V., Renaud, F., et al. 2014, ApJ, 780, 57
Brammer, G. B., van Dokkum, P. G., Franx, M., et al. 2012, ApJS, 200, 13
Bruzual, G., & Charlot, S. 2003, MNRAS, 344, 1000
Buck, T., Macciò, A. V., Obreja, A., et al. 2017, MNRAS, 468, 3628
Calzetti, D., Armus, L., Bohlin, R. C., et al. 2000, ApJ, 533, 682
Calzetti, D., Kinney, A. L., & Storchi-Bergmann, T. 1994, ApJ, 429, 582
Calzetti, D., Meurer, G. R., Bohlin, R. C., et al. 1997, AJ, 114, 1834
Ceverino, D., Dekel, A., & Bournaud, F. 2010, MNRAS, 404, 2151

Ceverino, D., Dekel, A., Mandelker, N., et al. 2012, MNRAS, 420, 3490
Ceverino, D., & Klypin, A. 2009, ApJ, 695, 292
Chabrier, G. 2003, PASP, 115, 763
Chan, J. C. C., Beifiori, A., Mendel, J. T., et al. 2016, MNRAS, 458, 3181
Conselice, C. J. 2003, ApJS, 147, 1
Conselice, C. J., Grogin, N. A., Jogee, S., et al. 2004, ApJL, 600, L139
Cowie, L. L., Hu, E. M., & Songaila, A. 1995, AJ, 110, 1576
Dahlen, T., Mobasher, B., Faber, S. M., et al. 2013, ApJ, 775, 93
Dekel, A., & Burkert, A. 2014, MNRAS, 438, 1870
Dekel, A., Sari, R., & Ceverino, D. 2009, ApJ, 703, 785
Dessauges-Zavadsky, M., Schaerer, D., Cava, A., Mayer, L., & Tamburello, V. 2017a, ApJL, 836, L22
Dessauges-Zavadsky, M., Zamojski, M., Rujopakarn, W., et al. 2017b, A&A, 605, 81
Elmegreen, B. G., Bournaud, F., & Elmegreen, D. M. 2008, ApJ, 688, 67
Elmegreen, B. G., & Elmegreen, D. M. 2005, ApJ, 627, 632
Elmegreen, B. G., Elmegreen, D. M., Fernandez, M. X., & Lemonias, J. J. 2009a, ApJ, 692, 12
Elmegreen, D. M., Elmegreen, B. G., Marcus, M. T., et al. 2009b, ApJ, 701, 306
Elmegreen, D. M., Elmegreen, B. G., Ravindranath, S., & Coe, D. A. 2007, ApJ, 658, 763
Elmegreen, D. M., Elmegreen, B. G., & Sheets, C. M. 2004, ApJ, 603, 74
Fioc, M., & Rocca-Volmerange, B. 1997, A&A, 326, 950
Fisher, D. B., Glazebrook, K., Abraham, R. G., et al. 2017a, ApJL, 839, 5
Fisher, D. B., Glazebrook, K., Damjanov, I., et al. 2017b, MNRAS, 464, 491
Förster Schreiber, N. M., Shapley, A. E., Genzel, R., et al. 2011, ApJ, 739, 45
Gabor, J. M., & Bournaud, F. 2013, MNRAS, 434, 606
Gargiulo, A., Saracco, P., & Longhetti, M. 2011, MNRAS, 412, 1804
Gargiulo, A., Saracco, P., Longhetti, M., La Barbera, F., & Tamburri, S. 2012, MNRAS, 425, 2698
Genel, S., Naab, T., Genzel, R., et al. 2012, ApJ, 745, 11
Genzel, R., Burkert, A., Bouché, N., et al. 2008, ApJ, 687, 59
Genzel, R., Newman, S., Jones, T., et al. 2011, ApJ, 733, 101
Grogin, N. A., Kocevski, D. D., Faber, S. M., et al. 2011, ApJS, 197, 35
Guo, Y., Ferguson, H. C., Bell, E. F., et al. 2015, ApJ, 800, 39
Guo, Y., Ferguson, H. C., Giavalisco, M., et al. 2013, ApJS, 207, 24
Guo, Y., Giavalisco, M., Cassata, P., et al. 2011, ApJ, 735, 18
Guo, Y., Giavalisco, M., Cassata, P., et al. 2012a, ApJ, 749, 149
Guo, Y., Giavalisco, M., Ferguson, H. C., Cassata, P., & Koekemoer, A. M. 2012b, ApJ, 757, 120
Hemmati, S., Miller, S. H., Mobasher, B., et al. 2014, ApJ, 797, 108
Hemmati, S., Mobasher, B., Darvish, B., et al. 2015, ApJ, 814, 46
Hinojosa-Goñi, R., Muñoz-Tuñón, C., & Méndez-Abreu, J. 2016, A&A, 592, A122
Hopkins, P. F., Kereš, D., & Murray, N. 2013, MNRAS, 432, 2639
Hopkins, P. F., Kereš, D., Murray, N., Quataert, E., & Hernquist, L. 2012, MNRAS, 427, 968
Hopkins, P. F., Kereš, D., Oñorbe, J., et al. 2014, MNRAS, 445, 581
Immeli, A., Samland, M., Gerhard, O., & Westera, P. 2004a, A&A, 413, 547
Immeli, A., Samland, M., Westera, P., & Gerhard, O. 2004b, ApJ, 611, 20
Inoue, S., Dekel, A., Mandelker, N., et al. 2016, MNRAS, 456, 2052
Inoue, S., & Saitoh, T. R. 2014, MNRAS, 441, 243
Jones, T. A., Swinbank, A. M., Ellis, R. S., Richard, J., & Stark, D. P. 2010, MNRAS, 404, 1247
Kennicutt, R. C., Jr. 1998, ARA&A, 36, 189
Kocevski, D., Barro, G., Faber, S. M., et al. 2017, ApJ, 846, 112
Koekemoer, A. M., Faber, S. M., Ferguson, H. C., et al. 2011, ApJS, 197, 36
Kravtsov, A. V. 2003, ApJL, 590, L1

Kravtsov, A. V., Klypin, A. A., & Khokhlov, A. M. 1997, ApJS, 111, 73
Kriek, M., van Dokkum, P. G., Labbé, I., et al. 2009, ApJ, 700, 221
Krumholz, M. R., & Dekel, A. 2010, MNRAS, 406, 112
Lang, P., Wuyts, S., Somerville, R. S., et al. 2014, ApJ, 788, 11
Lee, B., Giavalisco, M., Whitaker, K., et al. 2017, arXiv:1706.02311
Liu, F. S., Jiang, D., Guo, Y., et al. 2016, ApJL, 822, L25
Livermore, R. C., Jones, T., Richard, J., et al. 2012, MNRAS, 427, 688
Livermore, R. C., Jones, T. A., Richard, J., et al. 2015, MNRAS, 450, 1812
Madau, P. 1995, ApJ, 441, 18
Mandelker, N., Dekel, A., Ceverino, D., et al. 2014, MNRAS, 443, 3675
Mandelker, N., Dekel, A., Ceverino, D., et al. 2017, MNRAS, 464, 635
McGrath, E. J., Stockton, A., Canalizo, G., Iye, M., & Maihara, T. 2008, ApJ, 682, 303
Menanteau, F., Ford, H. C., Illingworth, G. D., et al. 2004, ApJ, 612, 202
Mieda, E., Wright, S. A., Larkin, J. E., et al. 2016, ApJ, 831, 78
Mobasher, B., Dahlen, T., Ferguson, H. C., et al. 2015, ApJ, 808, 101
Moody, C. E., Guo, Y., Mandelker, N., et al. 2014, MNRAS, 444, 1389
Mosleh, M., Tacchella, S., Renzini, A., et al. 2017, ApJ, 837, 2
Murata, K. L., Kajisawa, M., Taniguchi, Y., et al. 2014, ApJ, 786, 15
Murray, N., Quataert, E., & Thompson, T. A. 2010, ApJ, 709, 191
Nelson, E. J., van Dokkum, P. G., Förster Schreiber, N. M., et al. 2016a, ApJ, 828, 27
Nelson, E. J., van Dokkum, P. G., Momcheva, I. G., et al. 2016b, ApJL, 817, L9
Newman, S. F., Genzel, R., Förster-Schreiber, N. M., et al. 2012, ApJ, 761, 43
Noguchi, M. 1999, ApJ, 514, 77
Oke, J. B. 1974, ApJS, 27, 21
Oklopčić, A., Hopkins, P. F., Feldmann, R., et al. 2017, MNRAS, 465, 952
Puech, M. 2010, MNRAS, 406, 535
Puech, M., Hammer, F., Flores, H., Neichel, B., & Yang, Y. 2009, A&A, 493, 899
Ribeiro, B., Le Fèvre, O., Cassata, P., et al. 2017, A&A, 608, A16
Santini, P., Ferguson, H. C., Fontana, A., et al. 2015, ApJ, 801, 97
Saracco, P., Gargiulo, A., & Longhetti, M. 2012, MNRAS, 422, 3107
Shibuya, T., Ouchi, M., Kubo, M., & Harikane, Y. 2016, ApJ, 821, 72
Soto, E., de Mello, D. F., Rafelski, M., et al. 2017, ApJ, 837, 6
Straughn, A. N., Voyer, E. N., Eufrasio, R. T., et al. 2015, ApJ, 814, 97
Struck, C., & Elmegreen, B. G. 2017, MNRAS, 464, 1482
Swinbank, A. M., Smail, I., Longmore, S., et al. 2010, Natur, 464, 733
Szomoru, D., Franx, M., Bouwens, R. J., et al. 2011, ApJL, 735, L22
Szomoru, D., Franx, M., van Dokkum, P. G., et al. 2013, ApJ, 763, 73
Tacchella, S., Carollo, C. M., Forster Schreiber, N. M., et al. 2017, arXiv:1704.00733
Tacchella, S., Carollo, C. M., Renzini, A., et al. 2015a, Sci, 348, 314
Tacchella, S., Lang, P., Carollo, C. M., et al. 2015b, ApJ, 802, 101
Tadaki, K.-i., Kodama, T., Tanaka, I., et al. 2014, ApJ, 780, 77
Tamburello, V., Mayer, L., Shen, S., & Wadsley, J. 2015, MNRAS, 453, 2490
Tortora, C., Napolitano, N. R., Cardone, V. F., et al. 2010, MNRAS, 407, 144
Trump, J. R., Barro, G., Juneau, S., et al. 2014, ApJ, 793, 101
van den Bergh, S., Abraham, R. G., Ellis, R. S., et al. 1996, AJ, 112, 359
van der Wel, A., Franx, M., van Dokkum, P. G., et al. 2014, ApJ, 788, 28
van Dokkum, P. G., Bezanson, R., van der Wel, A., et al. 2014, ApJ, 791, 45
Wang, W., Faber, S. M., Liu, F. S., et al. 2017, MNRAS, 469, 4063
Whitaker, K. E., Franx, M., Leja, J., et al. 2014, ApJ, 795, 104
Wisnioski, E., Glazebrook, K., Blake, C., et al. 2011, MNRAS, 417, 2601
Wuyts, E., Rigby, J. R., Gladders, M. D., & Sharon, K. 2014, ApJ, 781, 61
Wuyts, S., Förster Schreiber, N. M., Genzel, R., et al. 2012, ApJ, 753, 114
Wuyts, S., Förster Schreiber, N. M., Nelson, E. J., et al. 2013, ApJ, 779, 135
Zanella, A., Daddi, E., Le Floc'h, E., et al. 2015, Natur, 521, 54